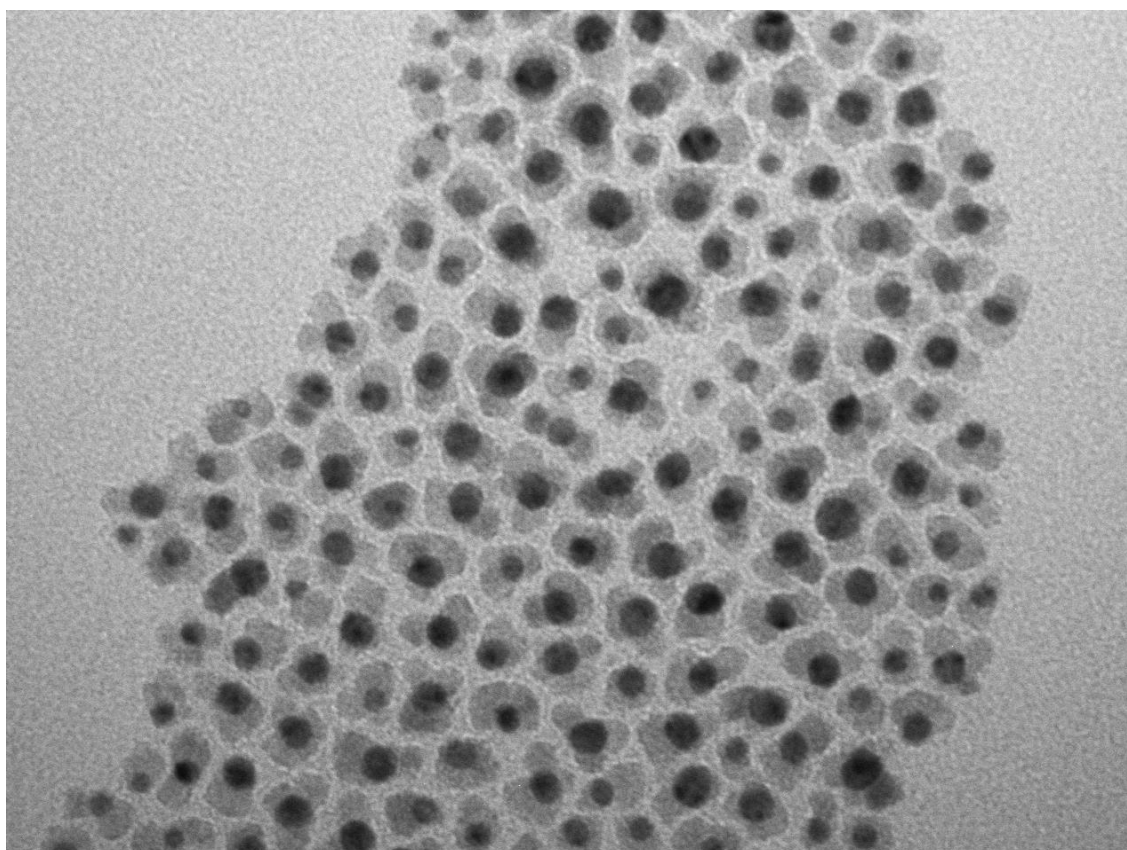UNIVERSITY
OF TRENTO - Italy
DEPARTMENT OF INDUSTRIAL ENGINEERING

XXVIII cycle

Doctoral School in Materials Science and Engineering

Development of Gold-Magnetite Hybrid Nanoparticles for Advanced Radiotherapy

Filippo Benetti

November 2015

DEVELOPMENT OF GOLD-MAGNETITE HYBRID NANOPARTICLES

FOR ADVANCED RADIOTHERAPY

Filippo Benetti

E-mail: Filippo.benetti@unitn.it

Approved by:

Prof. Claudio Migliaresi, Advisor

Department of Industrial Engineering

University of Trento, Italy.

Dr. Devid Maniglio, Advisor

Department of Industrial Engineering

University of Trento, Italy.

Ph.D. Commission:

Prof. Antonella Motta,

Department of Industrial Engineering

University of Trento, Italy.

Prof. Emanuela Cerri,

Department of Industrial Engineering

University of Parma, Italy.

Prof. Nuno M. Neves,

Department of Polymer Engineering

University of Minho, Portugal.

University of Trento,

Department of Industrial Engineering

November 2015

To my family

Abstract

The term "theranostics" defines the effort to develop individualized therapies by the combination of diagnostic and therapeutic functions in the same agent. Gold-magnetite hybrid nanoparticles (H-NPs) are proposed as innovative theranostic nanotools for imaging-guided radiosensitization of cancers. H-NPs are designed to exert a dual function: (i) to provide contrast enhancement in magnetic resonance imaging (MRI).and (ii) to enhance radiation effects in the cancer. The imaging and the radiosensitization potentialities of H-NPs arise from the superparamagnetic behaviour of magnetite and the large x-ray extinction coefficient of gold, respectively. Hybrid nanoparticles allows cancer theranostics as the biodistibution of nanoparticles can be tracked by MR imaging, providing a real-time picture of the cancer radiosensitivity profile and allowing precise modulation of radiotherapy.

The purposes of this work are to synthetize properly designed gold-magnetite hybrid nanoparticles and to provide preliminary *in vitro* evaluations about the potentialities of nanoparticles as MRI-contrast agents and radiosensitizers.

A novel method for the synthesis of hydrophilic and superparamagnetic Tween20-stabilized dumbbell-like gold-magnetite hybrid nanoparticles was set up. Morphology and chemical composition of nanoparticles were assessed by transmission electron microscopy, x-ray diffraction analysis and ion-coupled plasma optical emission spectroscopy. Colloidal stability and magnetic properties of nanoparticles were determined by dynamic light scattering and alternating field magnetometer.

The potentialities of H-NPs for MR imaging were studied using a human 4T-MRI scanner. Nanoparticles were proven to induce concentration-dependent contrast enhancement in T2*-weighted MR-images. The biosafety, the cellular uptake and the radiosensitization activity of H-

NPs were investigated in human osteosarcoma MG63 cell cultures and murine 3T3 fibroblasts, using specific bioassays and laser scanning confocal microscopy. The results evidenced that nanoparticles were taken up by cells without inducing any cytotoxic effects, even at high nanoparticle concentration. In addition, nanoparticles were proven to induce osteosarcoma-specific reduction of cell viability in clonogenic cell cultures treated with radiotherapy.

The experimental results confirmed the potentialities of H-NPs as theranostic tools for MRI-guided radiosensitization. Further studies are needed to confirm our findings and to identify other potential biological targets for MRI-guided radiosensitization.

Table of Contents

Preface

In this dissertation, a report of my PhD research activity is provided. The activity was carried out in the Biotech Lab, part of the Industrial Engineering Department, of the University of Trento (Italy), under the supervision of Prof. Claudio Migliaresi and Dr. Devid Maniglio.

The purpose of the work is to deliver a proof-of-concept about the suitability of gold-magnetite hybrid nanoparticles for MRI-guided radiosensitization. The activity involved the synthesis and the characterization of properly designed nanoparticles and the evaluation of the in vitro performances of nanoparticles as contrast agent and radiosensitizer.

In the first chapter, a brief of overview of the physico-chemical properties, the biological interactions and the main applications in cancer care of nanoparticles is reported. The discussion allowed the identification of the most prominent issues for the design of medical nanoparticles. In subchapter 2.1, the results of a previous work about the role of size and surface chemistry of gold nanoparticles on blood protein adsorption is briefly discussed. The details of this study are reported in Appendix.

In the second chapter, the state-of-art of the research about high-Z nanoparticles for radiotherapy enhancement is discussed. The physical and biological mechanisms of

nanoparticle radiosensitization are reported and the concept of theranostic radiosensitization is introduced.

The rationale and the aims of the research activity are declared in the third chapter, together with the outline of the experimental work.

In Chapter IV, the methods for the synthesis and the characterization of hybrid nanoparticles are presented. The results allowed the determination of the synthesis procedure for the production of hybrid nanoparticles with morphology and chemical composition suitable for our purposes.

The methods and the results arising from the study of the magnetic properties and the imaging potentialities of hybrid nanoparticles are reported in the Chapter V. In particular, the experiment performed using the human MRI-scanner is discussed.

In chapter VI, the biological assays aimed to evaluate the biosafety, the cellular uptake and the radiosensitizing activity of nanoparticles are presented.

General conclusions and final remarks are delivered in chapter VII.

Chapter I

General introduction on medical nanoparticles

1.1. Physico-chemical properties and medical potentialities of nanoparticles

Nanoparticles are particles of any shape with at least two dimensions in the size range from 1 to 100 nm[1]. Humanity has handled nanoparticles for millennia in order to obtain manufacts with superior mechanical performances or for artistic purposes. For instance, ancient Romans used to synthetize colloidal gold for glass staining because of its characteristic coloration[2]. The technological progress occurred in the last two centuries has allowed a detailed study of nanoparticles, revealing very peculiar physico-chemical properties and promoting the diffusion of nanoparticles in several applications ranging from electronics, optics, environmental technologies to medicine.

The physics of nanoparticles is significantly different from the physics of bulk materials as, at the nanoscale, size and geometry can affect the atomic processes responsible for the physical behaviour of materials. Therefore, unlike larger materials, nanoparticles exhibit a variety of size-dependent and shape-dependent properties. The fluorescent behaviour of quantum dots is a typical example of size-dependent properties of nanoparticles. Quantum dots are semiconductive nanoparticles that experience the so-called quantum confinement effect. This phenomenon arises from the nanometric confinement of electrons, which behave like in quantum well conditions breaking the valence and conductive bands and leading to the formation of quantized energy levels. The energy differences among the quantized levels are determined by the nanoparticle size in such way that properly designed semiconductive nanoparticles (quantum dots) can be used as fluorescent probes with size-tunable excitation and emission wavelength[3].

Size is fundamental also in the case of superparamagnetic nanoparticles. Superparamagnetism is a form of magnetism that occurs in ferromagnetic and ferrimagnetic materials under certain conditions. In particular, if the size of particles is sufficiently small, the magnetization can randomly flip direction under the influence of temperature. If an external magnetic field is applied, the magnetic momentum of nanoparticles are oriented in the direction of the field, however no residual magnetization is maintained when the external field is removed, as result of the

thermal flipping. Therefore, superparamagnetic nanoparticles can be magnetized like a paramagnet, although their magnetic susceptivity is comparable to that of ferromagnetic materials[4].

Shape is another parameter that could strongly affect the physical behaviour of nanomaterials. In particular, the optical properties of metal nanoparticles are well-known to be shape-dependent. Passing from bulk to nanometric materials, surface plasmon resonance (SPR) becomes the main mechanism responsible for the optical response of metals as bulk scattering is negligible for particles smaller than 50 nm. Surface plasmon resonance is due to the collective oscillations of free electrons, stimulated by electromagnetic waves with frequency in the resonance band of electron oscillations. The SPR band depends on the shape of nanoparticles as the oscillation modes of electrons may change changing the nanoparticle symmetry[5]. The shape-dependence of the SPR band is particularly interesting in the case of noble metal nanoparticles. In particular, the shape of gold nanoparticles can be tuned in order to obtain SPR absorption in a wide spectral interval ranging from the visible to the near-IR. For example, spherical gold nanoparticles exhibit SPR absorption in the green part of the visible spectrum, while the SPR band of rod-like nanoparticles is red-shifted. In Fig. 1, a pictorial representation of quantum effect, superparamagnetism and surface plasmon resonance is reported.
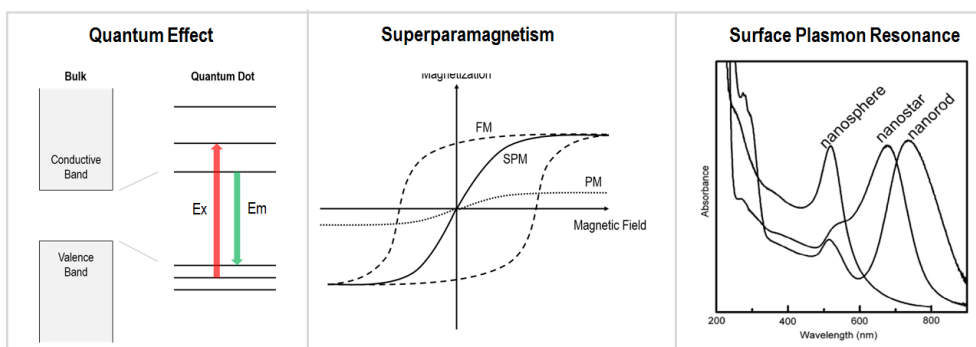
Figure 1. In the superparamagnetism box, FM, PM and SPM stand for ferromagnetic, paramagnetic and superparamagnetic materials, respectively.

Besides physics, nanoparticles differ from micrometric and millimetric material also for larger chemical reactivity. In fact, considering a typical atom size is about 1 Å, nanoparticles can be assumed as clusters of small number of atoms with a high percentage of surface atoms with unsaturated atomic orbitals. Although the large chemical reactivity of nanoparticles can result particularly useful for catalytic applications, the excess of surface energy makes nanoparticles thermodynamically unstable. Indeed, if the surface is not protected with stabilizing molecules, called capping agents, interactions between nanoparticles could occur in order to reduce the surface energy and this generally results in particle aggregation[6].

Recently, the opportunity to use nanoparticles for medical applications is object of intense scientific interest. In fact, nanoparticles provide the possibility to interact with the biological environment at the same size scale of the proteins, the smallest building blocks of the biological matter. Therefore, thanks to their biological mobility,

nanoparticles can reach biological targets impossible to achieve otherwise and their phyisico-chemical properties offer diagnostic and therapeutic opportunities that molecular drugs cannot provide. In particular, the size-dependent and the shape-dependent properties of nanoparticles can be finely tuned in order to exert specific medical functions. For examples, nanoparticles can be used as drug carriers, optical and magnetic absorbers for tissue ablation, imaging probes, contrast agents or magnetic nanoactuators[7,8]. In addition, the high surface-to-volume ratio of nanoparticles allows the conjugation of nanoparticles with specific molecules for better biological targeting and additional functionalities.

1.2. Biological interactions and toxicity concerns of medical nanoparticles

Nanoparticles for medical applications should be properly designed in order to promote favourable interactions with the biological environment where they are expected to operate. In particular, medical nanoparticles must be able to reach the biological targets in such a way to effectively deliver the treatment they are designed for, limiting the insurgence of adverse events. Following administration, nanoparticles interact first with the proteins in blood or in other extracellular fluids and, secondly, with cells in the tissues where they have been accumulated. Chemical composition, size and surface chemistry can strongly influence the way nanoparticles interact with proteins, cells and tissues determing nanoparticle toxicity and influencing the efficacy of the treatment. Therefore, the design of safe and effective medical nanoparticles requires a basic knowledge about the role of the size and the surface chemistry in the determination of the biological fate of nanoparticles. Considering that this work is aimed to develop medical gold-magnetite nanoparticles, the following discussion is mainly focused on gold and iron oxide nanoparticles.

Once in the bloodstream, nanoparticles interact with blood proteins and biomolecules generating a biological interface on the surface, called "corona". The

formation of such protein corona is a dynamic process. In general, for macroscopic materials, the surface is immediately covered by the most abundant blood proteins, which, in a second time, may be replaced by proteins with higher surface affinity. Previous works demonstrated the occurrence of exchange mechanisms also for metal nanoparticles[9]. The composition of the protein shell at equilibrium contributes to define the fate of nanoparticles and the occurrence of possible side effects. These could involve clearance of nanoparticles from the bloodstream, activation of complement cascade or thrombus formation[10]. Until now, very few studies have been carried out in order to obtain a complete comprehension about the occurrence of side effects due to the formation of unfavourable protein corona. In this contest, medical nanoparticles are generally designed to avoid as much as possible the amount of adsorbed proteins. The conjugation of nanoparticles with antifouling molecules could be a strategy to limit blood proteins adsorption. In particular, negative-charged long-chain molecules have been identified as a candidate for this purpose, as shown by a work of our research group[11]. The study was aimed to study the role of size and surface chemistry of gold nanoparticles on the process of blood protein adsorption. The details of the work are reported in Appendix. The experimental findings supported the belief that negative-charged nanoparticles, coated with the long-chain molecules, should behave better than other coatings in limiting the adsorption of blood proteins on the nanoparticle surface.

The interaction among nanoparticles and cells is another fundamental issue that should be considered in the design of medical nanoparticles. Due to the size difference, the nanoparticle-cell interactions often results in the cellular uptake of nanoparticles. Although some evidences highlighted that ultrasmall nanoparticles (< 10 nm) can enter into the cells by diffusion through the cell membrane, endocytosis has been identified as the principal mechanism for cellular uptake of nanoparticles[12]. Endocytosis involves the enclosure of the substances to be internalized by the cell membrane forming vesicles, which are furtherly released into the cytoplasm. Once in the cytoplasm, nanoparticle-loaded vesicles generally reach endomes and, in a later stage, lysosomes, where nanoparticles are degraded or excreted from the cell. Although Tkachenko et al. demonstrated the possibility to functionalize gold nanoparticles with specific peptides allowing nuclear targeting, nanoparticles generally cannot enter into the nucleous[13]. Endocytosis offers three main routes for nanoparticle internalization in cells: phagocytosis, macro-pinocytosis and receptor-mediated endocytosis[14]. Phagocytosis is a ligand-induced process, part of the immune system of animals, and is restricted to specialized cells, including macrophages, monocytes and neutrophils. Phagocytic cells can internalize cell debris, apoptotic cells and foreign bodies with diameter between 0.5 μm and 10 μm[15]. In non-phagocytic cells, nanoparticles can be internalized mainly by macro-pinocytosis, a nonspecific mechanism by which the compounds dispersed in the

fluid are taken up at the same concentration as in the surrounding medium. In addition, receptor-mediated endocytosis (RME), based on the activation of clathrin and claveolin pathways triggered by the binding of specific ligands, can occur. In Fig. 2, mechanisms of nanoparticle internalization by cells are summarized.
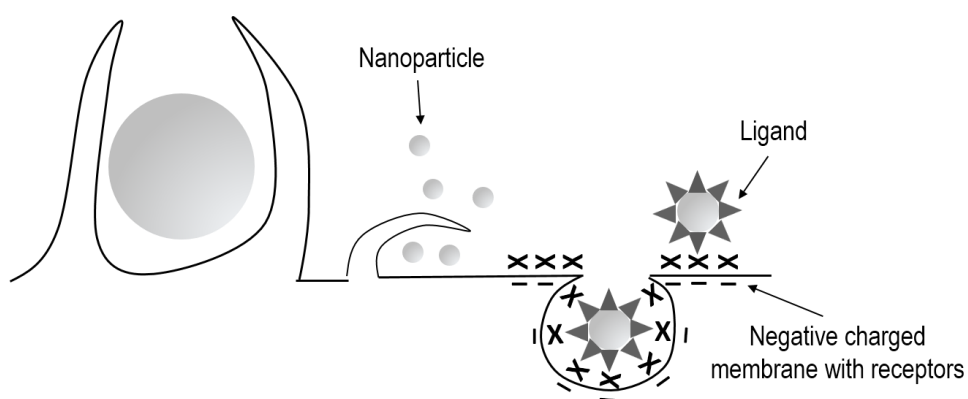
Figure 2. From left to right: particle uptake by phagocytosis, liquid internalization with included nanoparticles by macro-pinocytosis, specific binding of ligands to cell surface receptors and subsequent receptor-mediated endocytosis (RME).

The size of the vesicles formed by macro-pinocytosis and RME are limited and nanoparticles larger than 200 nm are typically unable to enter in non-phagocytic cells[16]. Moreover, nanoparticles in the size range from 40 nm to 50 nm were proven to be more efficient in cell internalization than smaller and larger nanoparticles[17].

Beside the size and the presence of specific ligands on the surface, other parameters of nanoparticles can affect the uptake process. In particular, increased charge, either positive and negative, favors the uptake in both phagocytic and non-phagocytic cells, and positively charged nanoparticles are taken up more extensively than negative ones, because of the negative potential of cell membrane[18,19].

Although the internalization of nanoparticles in cells is needed for several medical applications, nanoparticle uptake can lead to unwanted cytotoxicity. In fact, nanoparticles can affect the normal biological processes of cells by releasing degradation products into the cytoplasm or by generating reactive oxygen species. A great mole of studies has been conducted in the last years to determine the cytotoxicity effects of gold and iron oxide nanoparticles considering different cell types, nanoparticle size and surface chemistry, incubation time and concentrations. The studies were mainly based on the evaluation of cell integrity following incubation with nanoparticles *in vitro*. A review conducted by Lewinski et al showed that, in general, cells can survive to short-term exposure to gold and iron oxide nanoparticles at concentrations lower than 200 ug·mL^{-1}[20]. For higher concentrations, the occurrence of toxic effects strongly depends on certain nanoparticle parameters. In particular, positive charged nanoparticles resulted more cytotoxic than negative charged nanoparticles, probably because of the higher cellular uptake, with sligh dependency on the size[21]. Furthermore, the chemistry of surface coatings can

determine the occurrence of cytotoxic effects for the presence of specific chemical groups or for the lipophilic behaviour of certain capping agents.

Beside opsonisation and cytotoxicity, the pharmacokinetics and the biodistribution of nanoparticles represent another critical issue for the employment of nanoparticles in clinics. In fact, nanoparticles usually reveal faster clearance from the bloodstream compared to standard hydrophilic drugs and the biodistribution of nanoparticles can vary depending on the nanoparticle size. Several studies have investigated the biodistribution of gold nanoparticles intravenous-injected in rats examining different nanoparticle size and surface chemistry. The results highlighted that nanoparticles are quickly removed by the circulating system by the reticuloendothelian system (RES). The high efficiency of RES in nanoparticle clearance is probably due to the opsonisation of nanoparticles by blood proteins. In fact, nanoparticles capped with antifouling molecules, like PEG, exhibit longer circulating time compared to those with less stealth capacities[22]. Size is crucial in determining the accumulation profile of nanoparticles. In fact, as reported by Hirn et al, small nanoparticles, less than 6 nm, follow a different clearance routes than larger nanoparticles. In particular, small nanoparticles have longer retention time in blood tissue compared to larger nanoparticles and they are cleared mainly by kidney resulting in urine excretion. On the contrary, 24h clearance of larger nanoparticles occurs principally in liver and spleen leading to excretion by faeces. The circulating time of larger nanoparticles

scales with the inverse of size. Furthermore, small nanoparticles can be easily reach

organs like brain, lungs and heart[23]. Considering that gold nanoparticles are often

designed for cancer care applications, the role of size has been investigated in

terms of tumour accumulation. Perrault et al. studied the cancer uptake of PEG-

coated nanoparticles with different size in tumour bearing mice revealing that 60 nm

represents the optimal size to maximize PEG-coated nanoparticle accumulation in

cancer, probably as result of long circulating time and preferential cellular

internalization[24]. Furthermore, Fraga et al. studied the short-term (28 days) toxicity

of gold nanoparticles reporting that no significant change in food and water intake

and variation in organ indexes was detected following nanoparticle administration[25].

Although systematic studies about the pharmacokinetics and the biodistribution of

iron oxide nanoparticles are fewer than those about gold nanoparticles, iron oxide

nanoparticles have been recognized to behave similarly to gold nanoparticles in

terms of circulating time and tissue accumulation confirming that size and surface

chemistry are the principal parameters determining nanoparticle clearance and

biodistribution. In particular, nanoparticles larger than 10 nm are quickly cleared

from the bloodstream within 24 h and the clearance mainly occurs in liver and

spleen[26,27]. Moreover, no toxicity was detected in mice injected with iron oxide

nanoparticles at the concentrations typically used *in vivo* (~ 1 mg/kg)[28].

1.3. Cancer diagnostics, therapeutics and theranostics based on nanoparticles

Cancer care represents the most promising application field for medical nanoparticles. In the last decades, nanoparticles have been studied and developed primary for use in drug delivery systems (e.g. liposomes, gelatin nanoparticles, micelles) and, more recently, for therapeutic and diagnostic treatments exploiting the peculiar physico-chemical properties of metallic, semimetallic and carbon nanoparticles.

The suitability of nanoparticles for oncologic applications is supported by the evidence that macromolecules dispersed in the bloodstream are much more selective than low-molecular-weight molecules in targeting solid cancers. Selective accumulation of macromolecules in tumours is due to the enhanced permeability and retention of cancers (EPR effect) and arises from the higher density of blood vessels with defective architecture in tumours compare to normal tissue. The hyper-vascularization of cancers ensures a sufficient supply of nutrients and oxygen for a rapid growth and occurs at the first stages of tumour formation. In fact, when malignant cell aggregates reach the size of 0.8-1 mm, new vasculature starts to be generated as result of the extensive production of vasculature endothelial grow factors (VEGF) and other permeability factors. Cancer angiogenesis leads to the

formation of blood vessels with an abnormal structure, including large endothelial cell gap junctions ranging from 200 nm to 1.5 um, irregular vascular alignment, lack of smooth muscle layer and other defects. Although the high density of blood vessels induces an increase of fluid pressure in tumours, the architectural features of cancer vasculature allow the extravasation of macromolecules within the tumours. Furthermore, cancer tissues experience a lack a lymphatic drainage leading to longer retention of the compounds accumulated in the cancer compared to normal tissues[29,30]. In Fig. 3, a schematic description of EPR effect is reported.

Since the discovery of EPR effect in 1986, several strategies based on passive targeting have been developed. The first attempts involved the conjugation of standard low-molecular-weight chemotherapy drugs with high-molecular-weight molecules, like polymers or serum macromolecules. Furtherly, nanoparticles have been studied as novel carriers for hydrophobic anticancer drugs (e.g. doxorubicin), able to increase cancer selectivity reducing side effects. In fact, nanoparticles reveal superior stealth properties than other drug delivery systems limiting the unspecific drug uptake by RES[31]. Moreover, nanoparticles can perform active targeting of cancers by the conjugation with molecules able to bind tumour-specific ligands and several groups have reported the use of antibody-conjugated nanoparticles to localize cell surface proteins[32–34]. A lot of different nanoparticle formulations have been tested for anticancer drug delivery ranging from lipid-based liposomes,

micelles and polymersomes to protein-based, polymeric and mesoporous silica nanoparticles[35].
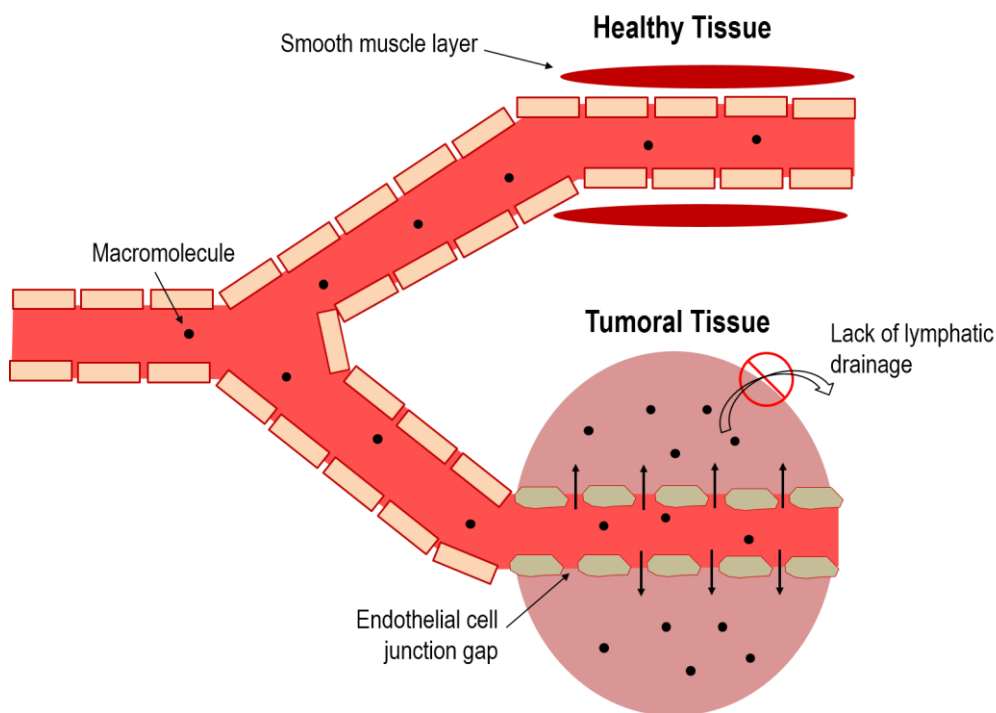
Figure 3. Macromolecules and nanoparticles dispersed in the bloodstream are selectively accumulated in the cancer tissue as result of large endothelial cell junction gaps and absence of smooth muscle layer in cancer vasculature. In addition, cancer tissue experiences lack of lymphatic drainage leading to longer retention of macromolecules and nanoparticles compared to normal tissues.

Metallic, semimetallic and carbon nanoparticles offer the opportunities to perform alternative cancer diagnostics and therapy thanks to their physico-chemical

properties. For instance, quantum dots have been developed for cancer applications in order to provide fluorescence imaging of subcutaneous cancers and carbon nanoparticles (e.g. fullerenes and carbon nanotubes) have been investigated for drug deliver, optical imaging and phototherapy. However, gold and iron oxide nanoparticles represent the most studied types of hard-matter nanoparticles for cancer care thanks to their unique features.

Gold nanoparticles were approved for the care of rheumatoid arthritis several decades ago and recently they have been studied as nanoplatforms for phototherapy, photoacoustic imaging, CT imaging and radiotherapy enhancement in cancers. The versatility of gold nanoparticles arises from the well-known biocompatibility of gold and the facile gold chemistry. In particular, the morphology of gold nanoparticles can be easily tuned in order to shift the surface plasmon resonance band in the near-IR range, where the optical absorption of biological tissues is minimal. Gold nanoparticles have been studied for phototherapy as the large optical absorption of gold nanoparticles can be used for cancer ablation or sensitization to further treatments[36,37]. Similarly, photo-acoustic tomography exploits the local pressure variations induced by the fast temperature increase following nanoparticle light absorption. In fact, if the exciting light is delivered by an ultrasound frequency pulsed laser, fast variations of pressure are generated inducing acoustic waves in the tissues. These waves can be detected from the skin and cancer

imaging is obtained by the reconstruction of the acoustic signals[38]. The limited

penetration depth of visible and near-IR light restricts the suitability of phototherapy

and photo-acoustic tomography to subcutaneous cancers. For deeper tumours, gold

nanoparticles have been studied as CT contrast agents and radiosensitizers. In fact,

thanks to the high extinction coefficient of high-Z materials for kilovoltage radiations,

gold nanoparticles are much more efficient than the biological matter in X-ray

absorption. The details about the interaction between gold nanoparticles and

ionizing radiations are discussed in the next chapter.

Superparamagetic iron oxide nanoparticles have been widely investigated since the

1980s for magnetic-targeted drug delivery, MRI contrast enhancement and

hyperthermia. Iron oxide nanoparticles are highly biocompatible and several groups

reported the synthesis of liposomes or polymeric particles loaded with

superparamagnetic nanoparticles for drug delivery in subcutaneous cancers by

magnetic targeting using a permanent magnet in proximity of the tumour [31,39]. *In vivo*

studies revealed magnetic carriers can improve drug delivery in cancer in terms of

selectivity and cancer regression[40–43].

Superparamagnetic nanoparticles have been also used as contrast agents in

magnetic resonance imaging (MRI). Magnetic resonance imaging provides

anatomical images of the body exploiting the magnetic relaxation processes of

protons in H^1 nuclei of the water molecules. The patient is placed in a strong static

magnetic field and the magnetic moments of H^1 protons aligned to the static field are flipped on the transverse plane using radiofrequency pulse at the Larmor precession frequency of protons. When the radiofrequency pulse is turned off, magnetic moments of flipped protons undergo to longitudinal relaxation (T1) and transverse relaxation (T2). The first involves the recovery of magnetization in the direction of static magnetic field. The second occur on the transverse plane and arises from the loss of phase coherence in the precession of protons due to their magnetic interactions with each other and with other fluctuating moments in the tissue. As dephasing can also be affected by local inhomogeneities in the applied longitudinal field, superparamagnetic nanoparticles can be used as negative contrast agents in T2-weighted MRI. In fact, the magnetization of superparamagnetic nanoparticles in the tissue can locally disturb the static magnetic field leading to a decrease of transverse relaxation time. Iron oxide nanoparticles have been used as superparamagnetic contrast agents instead of standard contrast agents based on gadolinium because of the superior biocompatibility of iron oxide. Commercial agents based on superparamagnetic nanoparticles are currently available, such as 'Feridex I. V', an iron oxide contrast agent marketed by Advanced Magnetics Inc. Properly designed superparamagnetic iron oxide nanoparticles have been studied for cancer imaging. For instance, polymer-coated nanoparticles functionalized with

targeting molecules have demonstrated to provide excellent contrast enhancement of cancer tissue *in vivo* experiment[44–46].

Furthermore, superparamagnetic iron oxide nanoparticles can be used for cancer hyperthermia. In fact, if nanoparticles are placed in an AC magnetic field, the processes occurring in magnetic moment reversal (mainly Brownian rotation and Néel relaxation) induce the generation of heat, which is transferred to the surrounding environment. Nanoparticles-based hyperthermia can be used for cancer therapy by infiltrating the tumours with superparamagnetic iron oxide nanoparticles and irradiating the cancer lesion with AC magnetic field at the proper frequency[47–49]. This approach has been demonstrated to provide significant benefits in terms of cancer regression and sensitization and MagForce GmbH, in Munich, currently deliver nanoparticle-based hyperthermia in oncologic patients by *in situ* injection of superparamagnetic iron oxide nanoparticles.

The versatility of nanoparticles allows the development of multifunctional nanoparticles able to combine imaging and therapeutic potentialities. Such nanoparticles provide the opportunity to test the patient response allowing the modulation of the treatment on the individual patient. People generally referred to medical treatments based on drugs or agents able to integrate therapeutic and prognostic purposes using the term "theranostics". Currently, theranostic treatments are object of intense scientific interest as the opportunity to module the therapy on

the needs of the individual patient represents the main target of personalized medicine, which is generally considered the next frontier of modern medicine[50]. In our group, theranostic iron oxide nanoparticles, functionalized with antibodies specific for endothelial grow factors receptor (EGFr), have been developed for real-time MRI-tracking of doxorubicin-loaded nanoparticle biodistribution in mice engrafted with human colorectal cancers. Other groups reported similar studies and the results support the feasibility of the cancer theranostics using superparamagnetic iron oxide nanoparticles for MRI-monitored drug delivery[51]. In addition, iron oxide, gold and gadolinium nanoparticles as well offered theranostic opportunities. In particular, iron oxide nanoparticles can be used for MRI contrast enhancement and hyperthermia, while gold and gadolinium nanoparticles have been studied for CT-guided and MRI-guided radiosensitization, respectively[52–54]. Furthermore, the development of hybrid nanoparticles has enlarged the possibilities offered by nanoparticles for cancer theranostics. For instance, Kirui et al reported a study regarding gold-iron oxide hybrid nanoparticles for MRI-guided phototherapy on tumor bearing mice[55] and Kim et al investigated the opportunities for MRI, fluorescence imaging and drug delivery of iron oxide nanoparticles coated by a shell of mesoporous silica[58]. Considering the increasing demand of personalized medicine and the potentialities of hybrid nanoparticles combined imaging and

therapy of cancers, more and more medical strategies based on theranostic hybrid nanoplatforms are expected to emerge in the next years.

Chapter II

Nanoparticles for advanced radiotherapy

2.1. Basic concepts about radiotherapy

Radiotherapy is the second most diffused treatment for cancers after surgery and more than half of oncologic patients are estimated to experience radiotherapy during their clinical management[57,58]. In particular, radiotherapy is the elected treatment for long-term control of head, neck, lung, cervix, bladder, prostate and skin cancers.

Radiotherapy employs ionizing photon radiations, delivered in the cancer site, in order to induce lethal damages in tumour cells. Radiation-induced cytotoxicity results from a succession of physical, chemical and biological processes. As first, incident photons interact with orbital electrons mainly by photoelectric effect and Compton scattering effect, resulting in the occurrence of ionization and excitation events. If sufficiently energetic, secondary electrons, ejected by ionization, interact with other orbital electrons giving rise to ionization/excitation cascades. The density of ionization/excitation events depends on the radiation dose deposited in the tissues, defined as the amount of energy released by radiations in a unit of mass.

Radiation dose is measured in Grays (Gy) and 1 Gy corresponds to 1 Joule per Kg of matter. The processes of ionization and excitation of molecules lead to the breakage of chemical bonds and formation of free radicals that rapidly react with the surrounding matter. Such chemical reactions result in the fixation of radiation damages leading to stable changes in biological molecules. For clinical radiation doses, the most part of radiation-induced lesions occurred in non-fundamental biomolecules which are easily replaced without relevant effects on cell behaviour. However, some lesions can occur in the DNA molecules, as consequence of direct damages due to ionization/excitation processes or indirect damages provoked by the interaction with free radicals. The vast majority of DNA lesions are successfully repaired by specific enzymatic reactions, however it could happen that some of them fail to repair. Such irreversible modifications could have severe effects in terms of cell viability and proliferation. In particular, DNA damages could induce cell death by apoptosis, necrosis and mitotic catastrophe or could induce replicative senescence depending on the cell type. As consequence of radiation-induced cell death, tumour regression occurs after irradiation, often followed by regrowth. If regrowth fails to occur during the lifespan of the patient, the cure of cancer, even called local control, is achieved. Due to the difficulty to confine the irradiation on the cancer site, also healthy tissues can be irradiated during radiotherapy. Healthy tissue irradiation could induce short-term and long-term side effects. In particular, the killing of stem cells

causes the early manifestations of normal tissue damage during the first weeks and months after irradiation. Examples are the breakdown of the skin or the mucosa, the denudation of the intestine and the hematopoietic damage. Furthermore, long-term effects include the appearance of second tumours induced by radiations, even after years from the irradiation[59,60]. Clinical practice guidelines define the dose level for the cancer local control and the insurgence of adverse events in the healthy tissues.

Radiotherapy equipment is usually composed by an electron linear accelerator with a tungsten alloy target at the end of the accelerating path. The collision among the pre-accelerated electrons and the tungsten target results in the generation of photons, via bremsstrahlung effect. The spectrum of the emitted photons follows a broad energy distribution, whose highest energy value corresponds to the acceleration energy of electrons. This value is called peak energy and is generally indicated in peak kilovolts (kVp) or peak megavolts (MVp). Radiotherapy systems allow the modulation of peak energy value by setting the electric potential across the linear accelerator. In the clinical practice, peak energy should be carefully tuned for optimal dose shaping as higher peak energy values correspond to higher penetration depth of the emitted photons in biological tissues. For instance, skin treatments generally imply peak energy values in the range from 100 kVp to 500

kVp, while peak energies between 1 MVp and 15 MVp are typically used in the treatment of deeper tissues.

The geometry of the photon beams is carefully tuned in order to optimize the dose deposition in the cancer preventing as much as possible healthy tissue irradiation. For this purpose, anatomical pictures offered by computer tomography (CT), positron emission tomography (PET) and MR imaging are used to plan radiation treatment. Several systems have been developed to improve the outcomes of radiotherapy. For instance, multiport irradiation method, based on multiple radiation beams delivered from different directions, has been implemented to provide better dose shaping. In addition, dose fractionation over a week or more is widely used to enhance cancer cell toxicity as normal cells generally recover faster than cancer cells.

However, radiotherapy of radioresistant cancers still remains challenging. For example, the local control of hypoxic tumours requires the deposition of larger radiation dose compared to normally-oxygenated tissues. In fact, hypoxia, due to the lack of blood supply in tumour tissue, induces cancer radioresistance as oxygen radicals are the most efficient chemical species for the fixation of radiation damages. To enhance cancer cell killing while minimally affecting healthy tissues, several pharmacological adjuvants for radiotherapy have been tested since the 1960s. A typical strategy for cancer radiosensitization involves the combination of

chemotherapy drugs (e.g. cisplatin, 5-fluororacil and mitomycin C) and radiotherapy in order to inhibit the DNA repair mechanisms following irradiation. Furthermore, a variety of radiosensitizing drugs have been designed to be activated by radiations and to target specific characteristics of tumours, like hypoxia. The majority of the hypoxia-specific radiosensitizers belongs to the family of nitroimidazoles that selectively target hypoxic cells and mimic the effect of oxygen in the fixation of DNA damages. However, selectivity still remains the main limitation for clinical implementation of radiosensitizers[61,62]. In this contest, innovative tools for radioresistant cancer sensitization are strongly demanded.

2.2. High-Z nanoparticles for radiotherapy enhancement

In the recent years, nanoparticles composed by high atomic number materials (high-Z nanoparticles) have been proposed as alternative platforms for selective cancer radiosensitization. As discussed in Chapter I, properly designed nanoparticles can target cancer tissue exploiting the architectural defects of tumour vasculature. In particular, the enhanced permeability and retention effect (EPR) occurring in cancer tissues allows passive targeting of cancers. Normal tissues are usually impermeable to nanoparticle infiltration and nanoparticles are quickly cleared from the bloodstream by filtering organs. Therefore, nanoparticles can provide higher cancer selectivity than standard low-molecular-weight drugs with minimal long-term accumulation in the healthy tissues.

Currently, high-Z nanoparticles have been studied to enhance the deposition of radiation dose in cancer tissue combining the targeting properties of nanoparticles and the large x-ray absorption of heavy materials. In fact, high-Z materials present higher extinction coefficient compared to the biological matter for photons in the kilovoltage energy range, as shown in Fig. 4.
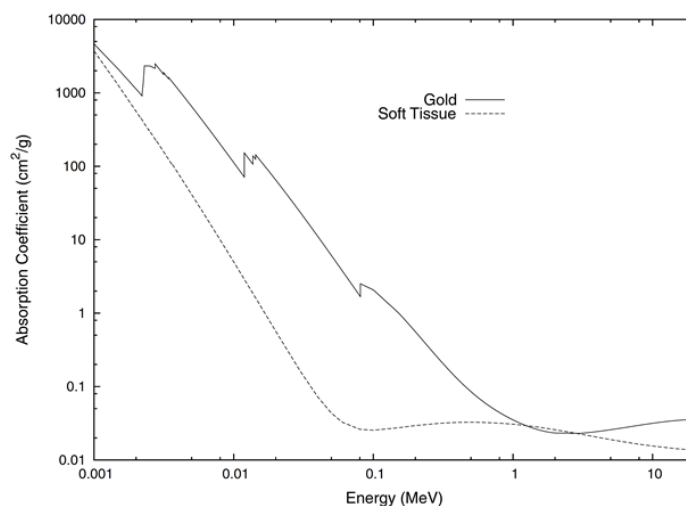
Figure 4 Comparison among the absorption coefficient of gold and soft tissue for photons in the energy range from 10 keV to 15 MeV[63].

The interaction among x-rays and heavy atoms results in the generation of low-energy secondary electrons by Auger effect and photoelectric effect. Secondary electrons release all their energy at sub-micrometer distance inducing the formation of free radicals at short range. Therefore, kilovoltage irradiation leads to the formation of free radicals at high density around high-Z nanoparticles, as confirmed by Monte Carlo studies[64,65] The local inhomogeneities in radiation dose deposition induced by nanoparticles could enhance cell killing probability. In fact, although nanoparticles are not incorporated within cell nuclei, the local dose inhomogeneities can disrupt lethal cytoplasmic targets (e.g. mitochondria), as shown in Fig. 5. In case of megavoltage photon irradiation, the extinction coefficient of high-Z materials and

the biological matter are quite similar. Although this evidence might suggest lack of radiosensitizing potentialities, computational studies demonstrated high-Z nanoparticles provide radiotherapy enhancement even in megavoltage energy range[66]. In fact, the interaction of primary megavoltage radiations with the matter results in the formation of secondary photons at lower energy, as consequence of Compton scattering. Secondary photons can interact with high-Z nanoparticles inducing local dose inhomogeneities, similarly to the case of kilovoltage radiotherapy. Therefore, high-Z nanoparticles are reliable platforms for the enhancement of both kilovoltage and megavoltage radiotherapy.
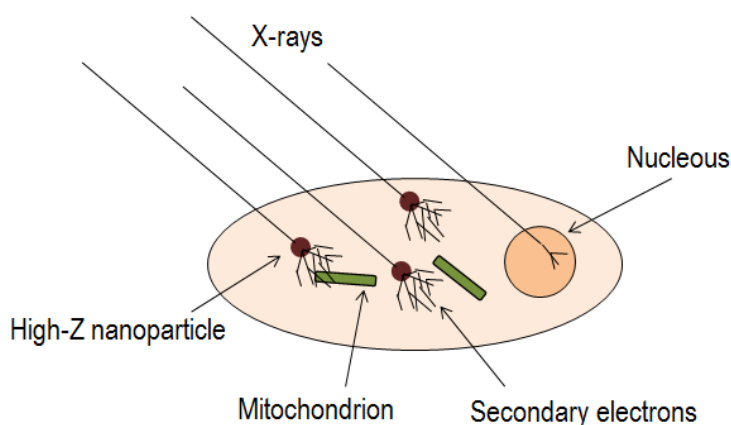

Figure 5 High-Z nanoparticles enhance radiation toxicity in cells by inducing sub-micrometer inhomogeneities in radiation dose deposition. In particular, nanoparticles release a huge amount of secondary electrons in the surroundings. This leads to a dramatic increase of the oxidative stress at short-range that may damage lethal cytoplasmic targets, like mitochondria.

Gold nanoparticles have been widely studied for radiosensitization due to their biocompatibility and facile chemistry. In 2004, the pioneering work of Hanfield et al reported the *in vivo* use of gold nanoparticles for cancer sensitization to radiotherapy[67]. Mice bearing subcutaneous EMT-6 mammary carcinoma received a single intravenous injection of 1.9 nm diameter gold nanoparticles and they were then irradiated by 250 kVp x-rays. One-year survival was 86% versus 20% with x-rays alone and 0% with gold alone. More recent *in vitro* and *in vivo* studies confirmed the ability of gold nanoparticles to increase cell killing and tumour regression in megavoltage radiotherapy[68,69]. In particular, the studies highlighted the sensitization offered by gold nanoparticles is cell-specific with comparable effects at kilovoltage and megavoltage energies, and gold nanoparticles do not enhance DNA double-strand breaks as expected from nanoparticles segregated in cytoplasmic compartments. The size of gold nanoparticles can also play a fundamental role in the determination of the radiosensitization effects. Zhang et al reported a comparative study aimed to determine the most suitable size of gold nanoparticles for radiosensitization. Among nanoparticles of 4.6, 12.1, 27.3 and 46.6 nm diameter, 12.1 and 27.3 nm nanoparticles resulted the most efficient in reducing cell surviving fraction *in vitro* and in limiting tumour expansion in mice[70].

In the last years, other types of high-Z nanoparticles have been proposed for nanoparticle-mediated radiosensitization. In particular, gadolinium nanoparticles

have been investigated for radiotherapy enhancement as gadolinium has significant higher absorption coefficient than soft tissues for kilovoltage x-rays and provide MR imaging contrast. The combination of imaging properties and high atomic number suggested the use of gadolinium nanoparticles for the implementation of imaging-guided radiosensitization, as discussed in the following section.

2.3. Theranostic nanoparticles for imaging-guided radiosensitization

Precise modulation of drug-enhanced radiotherapy requires the accurate determination of radiosensitizer distribution in the cancer. In fact, local changes could occur in the accumulation of radiosensitizing drugs in cancer tissue leading to heterogeneous levels of sensitization across the tumour. The lack of non-invasive imaging techniques for the estimation of drug biodistribution is therefore a severe limitation for the standardization of conventional radiosensitizers.

Attempts to develop molecular drugs for combining real-time imaging and radiotherapy enhancement has included the development of radioactive iodine-based molecules able to target specific types of cancer (e.g. prostate)[71]. However, the unsafety of radioactive compounds and the difficulty to translate drug cancer selectivity in other types of tumours hinder the clinical diffusion of molecular drugs for theranostic radiosensitization.

In this contest, nanoparticles have been identified as promising theranostic tools for imaging-guided radiotherapy. In fact, thanks to their versatility, multifunctional nanoparticles can be developed for cancer targeting, real-time imaging and cell sensitization to radiations. Iron oxide nanoparticles have been studied as platforms able to integrate imaging and radiosensitization. In fact, iron oxide nanoparticles are MRI-contrasted and nanoparticle biodistribution can be tracked in real-time after

administration. In addition, iron oxide nanoparticles can be loaded with radiosensitizing drugs (e.g. cisplatinium) for cancer radiosensitization[72,73].

More recently, gadolinium nanoparticles have been tested *in vivo* for imaging-guided radiosensitization. In 2011, Le Duc *et al* investigated the opportunity to use gadolinium oxide core and polysiloxane shell nanoparticles for MR imaging and radiotherapy enhancement in brain-tumour bearing mice[74]. Contrast enhancement in T1-weighted MR images provided an accurate picture of the nanoparticle distribution in the cancer allowing the determination of the optimal timing for treatment delivery in order to maximize the radiosensitization effect offered by nanoparticles. The survival time of mice treated with gadolinium nanoparticles and radiotherapy was statistically longer compared to mice treated with radiotherapy only. A further work of Dufort *et al* investigated the theranostic potentialities of ultrasmall nanoparticles composed by a polysiloxane matrix filled with gadolinium chelates[75]. Nanoparticles were administrated via inhalation in mice bearing intrapulmonary-inoculated lung cancers. After administration, ultrashort echo-time MRI sequences and bioluminescence assays confirmed selective nanoparticle accumulation in cancer cells. Synergic effect of nanoparticles and radiotherapy was detected in terms of survival time increase in mice.

Gold nanoparticles have been proposed for imaging-guided radiosensitization. In 2013, Joh et al reported a study regarding PEG-coated injected in sarcoma-

implanted mice for CT tumour shaping and radiosensitization[53]. Gold nanoparticles provided excellent CT contrast allowing the precise definition of tumour volume. In addition, the administration of nanoparticles in combination with radiotherapy allowed larger regression of tumour volume compared to radiotherapy or nanoparticles only. Mice treated by nanoparticles and radiations survived much longer than those treat only by radiotherapy.

Considering the heterogeneity of experimental conditions among the works reported above (e.g. tumour type, radiation dose and energy, nanoparticle administration mode) and the absence of comparative studies in literature, it is extremely difficult to compare the theranostic performances of different types of nanoparticles and to draw reliable conclusions. In particular, universally accepted parameters to quantify the overall efficacy of nanoparticles considering both imaging power and radiosensitization potentialities still miss. However, some considerations may be drawn. Firstly, gold and gadolinium nanoparticles appear much more promising for theranostic radiosensitization than iron oxide nanoparticles as they can provide remarkable radiotherapy enhancement without any additional chemotherapy drug. Furthermore, gold nanoparticles have been reported to induce higher cell sensitization to radiations than gadolinium nanoparticles as gold nanoparticles scatter radiations more efficiently than gadolinium nanoparticles[76]. In fact, gold nanoparticles have larger scattering cross-section because Au (Z=79) is heavier

than Gd (Z=64) and atom packing is higher in gold nanoparticles than in gadolinium ones. On the other side, gadolinium nanoparticles allow real-time imaging by MRI, which is completely safe and non-invasive, while gold nanoparticles require the utilization of CT. Although the dose required for a single CT scan can be well-tolerated, repeated scans over short time intervals may induce high probability of secondary tumour insurgence, especially in radiotherapy patients that are already exposed to high radiation doses. Therefore, real-time tracking of gold nanoparticles is more problematic if compared to gadolinium nanoparticles. Some studies reported the use of gadolinium-coated gold nanoparticles for dual CT and MR imaging, but they did not investigate the opportunity to use such nanoparticles for imaging-guided radiosensitization combining the safety of MR imaging and the high radiosensitization offered by gold[77–79].

Chapter III

Rationale, aims and organization of the research activity

Previous studies reported the opportunity to use gadolinium nanoparticles and gold nanoparticles as theranostic nanoplatforms for imaging-guided radiosensitization. Beside the promising results, both nanoparticle types still present some limitations. In particular, gadolinium nanoparticles induce limited cell radiosensitization due to the low atomic number and atom packing density, while gold nanoparticles require the employment of CT imaging for nanoparticle-tracking with severe safety concerns for radiotherapy patients. In this work, gold-magnetite hybrid nanoparticles (H-NPs) are proposed as innovative agents for MRI-guided radiosensitization by combining the imaging properties of superparamagnetic magnetite and the radiosensitization potentialities offered by gold. As reported in Fig. 6, H-NPs are designed to infiltrate cancer tissue by passive targeting after intravenous injection. Following administration, nanoparticle biodistribution can be real-time monitored through the MRI-contrast enhancement offered by nanostructured magnetite. The imaging data should provide precise indications about the time evolution and the spatial profile of cancer radiosensitivity, enhanced by the gold contained in H-NPs. The real-time

picture of radiosensitivity profile across the tumour should allow the identification of the optimal time-point and dose shape for the optimization of the radiotherapy outcomes. The combination of safe real-time MR imaging and high-performance radiosensitization in a unique nanotool is expected to allow the personalization of radiotherapy together with a significant reduction of the radiation dose required for the local control of solid cancers compared to standard radiotherapy. This novel theranostic approach to radiotherapy claim to provide remarkable advances in the care of a wide range of solid radioresistant cancers with vasculature characteristics suitable for nanoparticle passive targeting.

The purpose of this work is to demonstrate the suitability of hybrid nanoparticles for MRI-guided radiosensitization. In particular, the aims of the project include i) the development of a reproducible synthesis method for the production of cheap, properly-sized, well-dispersed and superparamagnetic gold-magnetite hybrid nanoparticles that match the requirements for cancer passive targeting, and ii) the *in vitro* testing of such nanoparticles for MRI-imaging and radiosensitization at the concentrations typically used in nanomedicine using a human 4T-MRI scanner and cell lines, selected as a model of radioresistant cancer (osteosarcoma).
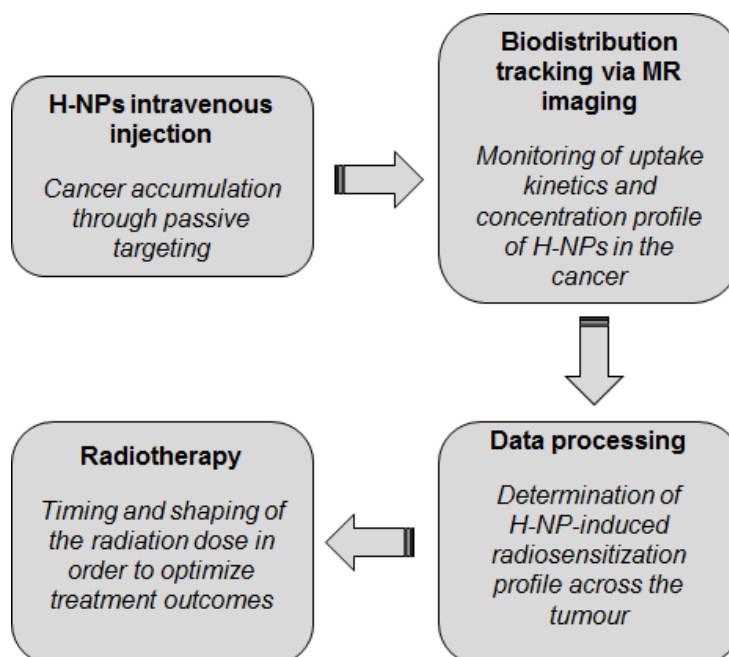
Figure 6. Schematic representation of the proposed theranostic treatment for MRI-guided radiosensitization.

To address these goals, the experimental work has been divided in three main steps:

1) Synthesis of gold-magnetite hybrid nanoparticles by two different methods. The physico-chemical characterization of the nanoparticles was carried out and the results allowed the determination of the synthesis method for the production of most suitable gold-magnetite hybrid nanoparticles for our purposes. In particular, size and chemical composition of the resulting

nanoparticles were used as parameters for the selection of the synthesis method.

2) Estimation of the magnetic properties of the gold-magnetite hybrid nanoparticles selected in the previous step. Nanoparticles were also tested in a 4T-MRI scanner approved for humans in order to assess the imaging potentialities of nanoparticles in the view of theranostic applications.

3) Evaluation of cytotoxicity, cellular uptake and *in vitro* radiosensitization of the selected hybrid nanoparticles using human osteosarcoma MG63 cells and murine embryonic fibroblast NIH-3T3 cells.

The experimental findings highlighted novelties in the field of nanoparticle chemistry regarding the production of hybrid nanoparticles suitable for cancer applications. Furthermore, the *in vitro* evaluations of the theranostic potentialities of our nanoparticles allowed preliminary considerations about the suitability of gold-magnetite hybrid nanoparticles for MRI-guided radiosensitization. An extensive discussion of the findings of this work is delivered in the final chapter.

Chapter IV

Synthesis and characterization of gold-magnetite hybrid nanoparticles

Two synthesis methods were tested for the production of hydrophilic gold-magnetite hybrid nanoparticles (H-NPs).

The first one involved the reduction of gold(III) chloride by hydroxylamine in presence of prefabricated iron oxide nanoparticles in alkaline solution. In our previous study[80], hydroxylamine-mediated gold reduction was demonstrated to induce the formation of gold star-shape nanostructures. Here, a similar procedure is used to synthetize H-NPs assuming that prefabricated iron oxide nanoparticles are embedded in the gold nanomatrices during gold growth process.

The second synthesis method was based on a two-steps process. As first, oil-soluble H-NPs were produced by thermal decomposition of metal precursors in a high-boiling point oil solution. Then, nanoparticles were dispersed in water by an innovative procedure based on polyoxyethylene(20) sorbitan monolaurate micelles.

Polyoxyethylene(20) sorbitan monolaurate is a non-ionic surfactant commonly used in a wide range of pharmacological applications and is known to be relative not-toxic. The commercial name of polyoxyethylene(20) sorbitan monolaurate is Tween20. The chemical structure is reported in Fig. 7. The hydrophilic head is composed by polyethylene glycol moieties conjugated to a sorbitan, while the hydrophobic tail is a molecule of lauric acid.
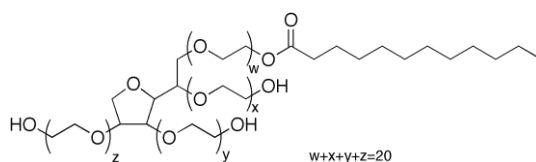

Figure 7. Chemical structure of Tween20.

Morphology and chemical composition of nanoparticles produced by both synthesis methods were determined using transmission electron microscopy (TEM), energy dispersive x-rays analysis (EDXA), X-ray diffraction spectroscopy (XRD) and ion-coupled plasma optical emission spectroscopy (ICP-OES). The hydrodynamic diameter in water and PBS solution of H-NPs synthetized by thermal decomposition method was evaluated by dynamic light scattering (DLS). Colloidal stability in protein solution was studied by the analysis of the optical absorption spectrum of nanoparticles at different time-points following nanoparticle incubation in cell culture medium. In fact, several experimental and theoretical studies have demonstrated that aggregation of plasmonic nanoparticles results in red shift and broadening of

plasmon absorption peak[81,82]. Unlike the case of DLS, the study of colloidal stability in protein solution by UV-visible spectroscopy does not require any purification steps that could perturb the final results. Therefore, UV-visible spectroscopy, although less informative, was preferred to DLS.

The experimental results allowed the identification of the most suitable synthesis method for the production of nanoparticles appropriate for our purposes.

4.1. Materials and methods

Chemicals

All the chemicals were of reagent grade and were used without any further purification. 1-Octadecene (technical grade 90%), oleic acid (90%), oleylamine (70%), iron(III) acetylacetonate (97%), 1,2-hexadecanediol (90%), gold(III) chloride trihydrate (≥ 99.9%), sodium hydroxide, iron pentacarbonyl (99.99%), Tween20, alcohol isopropyl (≥99.8%), ethanol (99%), toluene, dimethyl sulfoxide (99%) and cyclohexane were purchased by Sigma Aldrich. Methoxy-terminated 1,2-distearoyl-phosphatidylethanolamine-methyl-polyethylene glycol, MW 2500 Da, was purchased by Avanti Polar Lipids. Hydroxylamine hydrochloride (97%) was provided by Janssen Chimica. MG63 culture medium was prepared as described in Chapter VI. Below, the list of the abbreviations is reported.

Compound	Abbreviation
1-Octadecene	ODE
Oleic acid	OA
Oleylamine	OY
Iron(III) acetylacetonate	Fe(acac)
Iron pentacarbonyl	$Fe(CO)_5$

Dimethyl sulfoxide	DMSO
Methoxy-terminated 1,2-distearoyl-phosphatidylethanolamine-methyl-polyethylene glycol (MW 2,500 Da)	DSPE-mPEG

Hydroxylamine-based synthesis of H-NPs

This method involved three main synthesis steps.

1) Hydrophobic iron oxide nanoparticles were synthetized following the procedure reported by Sun et al[83]. A solution containing 700 mg Fe(acac), 2.6 g 1,2-hexadencadiol, 2 ml OA, 2 ml OY and 20 ml ODE was stirred and heated to reflux under a nitrogen blanket. Initially, the solution was heated to 200°C for 2 hours in order to promote thermal decomposition of Fe(acac), iron reduction by OY and nucleation of iron(0) atoms. Then, the solution was heated to 315°C for 1 hour to induce iron growth on the iron seeds. The solution was cooled down to room temperature maintaining the nitrogen blanket. One hour of air exposure was performed to allow iron oxidation. Furtherly, nanoparticles were flocculated by isopropyl alcohol, pelleted by centrifugation (30 min @ 6,000 rpm) and suspended in toluene. Toluene-dispersed nanoparticles were flocculated by ethanol, pelleted by

centrifugation and suspended in toluene. The process was repeated three times.

2) Phase transfer of iron oxide nanoparticles from the oil phase to water was performed using DSPE-mPEG micelles, as reported by Tong et al[84]. A solution of 2.4 ml chloroform containing DSPE-mPEG (0.5 mg/ml) was mixed to 0.6 ml magnetite nanoparticles (5 mg/ml). Under nitrogen blanket, 12 ml DMSO was gradually added under stirring. Then, chloroform was evaporated under nitrogen flux and 24 ml water was gradually added to the solution. Nanoparticles were purified by filtration (0.2 μm cellulose filter) and centrifugation (1h @ 40,000 rpm) in order to remove empty DSPE-mPEG micelles and nanoparticle aggregates.

3) Gold-magnetite hybrid nanoparticles were obtained by dropwise addition of hydroxylamine in a alkaline solution of gold(III) chloride, sodium hydroxide and DSPE-mPEG-stabilized iron oxide nanoparticles. The details of the procedure is covered by a European patent (WO 2014122608 A1). The resulting H-NPs were purified by magnetic separation and centrifugation to remove residual reagents.

Thermal decomposition synthesis of H-NPs

Oil-soluble H-NPs were synthetized as reported by Yu et al[85]. Briefly, a mixture of 20 ml ODE, 2 ml OA, 2 ml OY and 2 g 1,2-hexadecanediol was heated to reflux at 190°C under nitrogen blanket for 20 min. Then, 0.3 ml $Fe(CO)_5$ was added and, after 3 min, a solution of 40 mg gold(III) chloride dispersed in 5 ml ODE and 0.5 ml OY was poured in the mixture. Immediately after gold addition, the solution turned to red color as gold seeds formed. The solution was heated for 45 min at 315°C allowing the growth of the magnetite nanocrystal on the surface of the gold. In Fig. 8, a picture of the synthesis apparatus is reported. At the end of the process, the solution was cooled down to room temperature under nitrogen flow and 1h air exposure was performed to allow iron oxidation. The resulting nanoparticles were purified several times by flocculation (isopropyl alcohol and ethanol) and centrifugation (30 min @ 6,000 rpm). Finally, H-NPs were suspended in 20 ml toluene.

The oil-to-water transfer of H-NPs was carried out following a modified version of the procedure developed by Jin et al[86]. An aliquot of 5 ml H-NP solution was precipitated by centrifugation (30 min @ 6,000 rpm) after ethanol-induced flocculation and suspended in 1.0 ml cyclohexane. Then, the H-NP solution was added to 30 ml water and 150 µl Tween20. The mixture was sonicated for 20 min with a tip sonicator and placed at 85°C under nitrogen blanket for about 2 hours to evaporate

the cyclohexane. The resulting hydrophilic Tween20-capped H-NPs were purified by centrifugations (1h @ 20,000 rpm) and filtration.
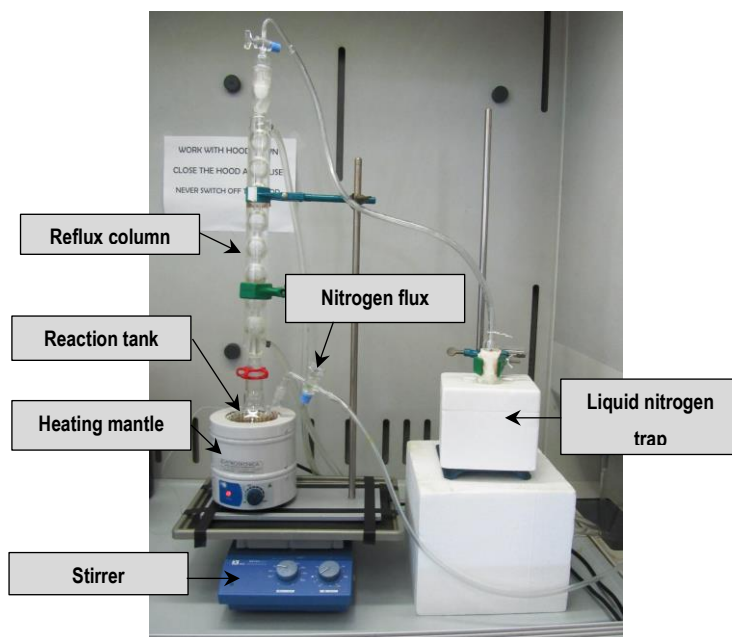

Figure 8. Experimental apparatus for the synthesis of hydrophobic H-NPs. The same apparatus was used for the synthesis of hydrophobic iron oxide nanoparticles.

Nanoparticle characterization

The morphology and the elemental composition of nanoparticles were studied using a Philips CM12 transmission electron microscope (TEM) operated at 120 kV and equipped with a system for energy-dispersive X-rays analysis (EDXA). Drops of

nanoparticle solutions were placed on carbofilm-coated copper grids and the solvents were evaporated before the analysis.

XRD analysis was performed on a thick layer of iron oxide nanoparticles and thermodecomposition-synthetized H-NPs, deposited on a silicon substrate, to study the crystalline structure of nanoparticles. The analysis was carried out using an Ital Structures APD2000 XRD instrument, in the parallel beam configuration.

The metal composition of both types of H-NPs was obtained by dissolving nanoparticles in aqua regia and analysing the dissolved solutions by a Spectro Ciros ICP-OES. The analysis was repeated for each synthesis batches to assess the reproducibility of the process.

Hydrodynamic diameter of Tween20-stabilized nanoparticles in water and phosphate-buffer (PBS) solution was acquired by a Zetasizer ZS dynamic light scattering (Malvern).

The evaluation of colloidal stability of Tween20-stabilized nanoparticles in protein solution was performed by incubating nanoparticles in MG63 cell culture medium for two days @ 37°C. Aliquots were withdrawn at different time-points (0h, 2h, 6h, 24h and 48h) and the optical absorption spectra were acquired by Tecan Microplate Reader. The absorption spectrum of nanoparticles dispersed in PBS was acquired for comparison.

4.2. Results

Iron oxide nanoparticles were produced for being used as reagent in the further synthesis of H-NPs. In the left part of Fig. 9, the characterization of the morphology and crystalline structure of oil-soluble iron oxide nanoparticles is reported. The transmission electron micrograph (Fig. 9A) confirms the formation of cubic-like nanostructures with average side length of 8.6 nm, as shown by the numerical size distribution (Fig. 9C). The XRD analysis (Fig. 9E) conducted on iron oxide nanoparticles confirms the achievement of magnetite nanocrystals. The large contribution of the amorphous phase arises from the OA-shell surrounding iron oxide nanoparticles[87]. The nanoparticles were furtherly transferred in water by DSPE-mPEG micelles and used as reagents for the synthesis of hybrid nanoparticles by hydroxylamine-mediated gold reduction in alkaline solution. The TEM image of the synthesis products (Fig. 9B) assesses the formation of gold-based nanostars with average diameter of 63 nm, as shown by the numerical size distribution (Fig. 9D). The EDXA spectrum (Fig. 9F) confirms the presence of iron and gold in the sample, although the iron signal is almost negligible.
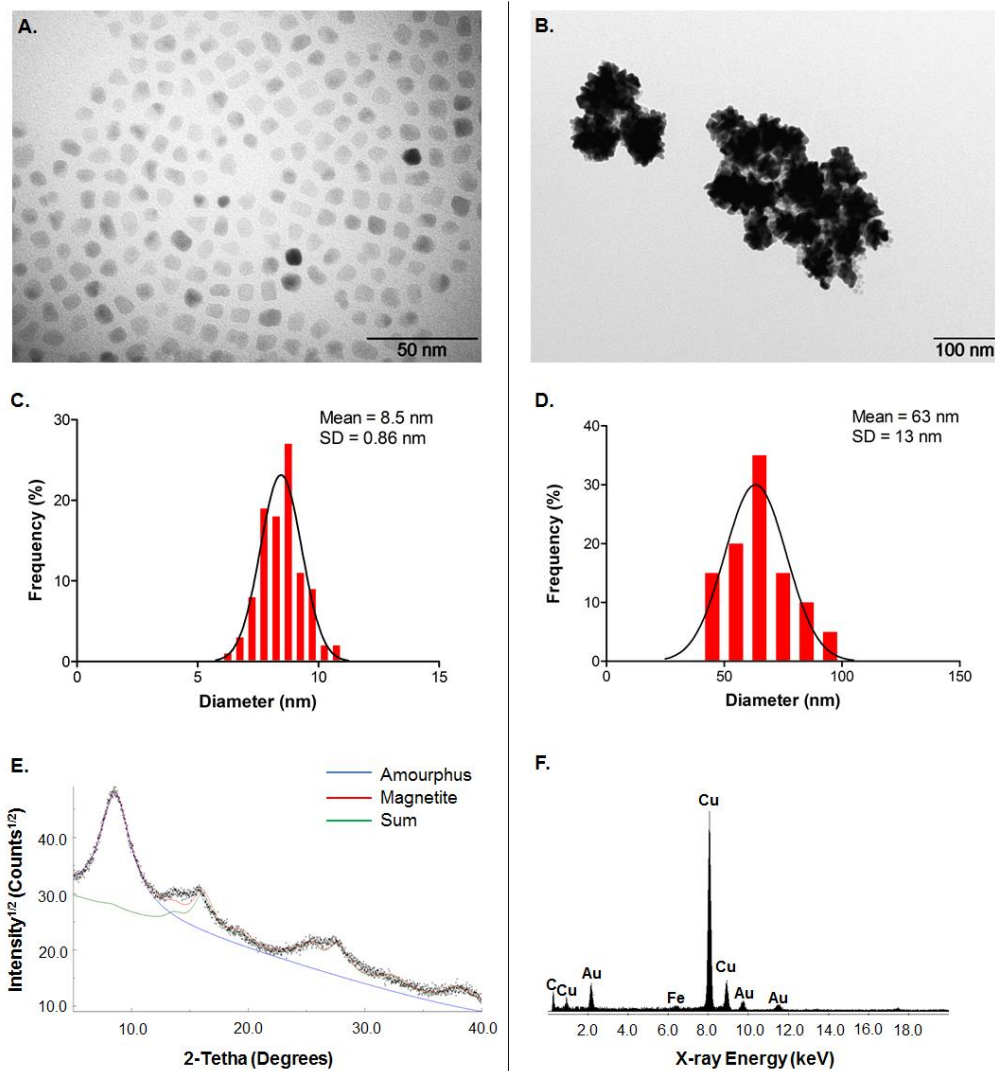
Figure 9. Morphological and chemical characterization of oil-soluble iron oxide nanoparticles (left) and hybrid nanoparticles produced by hydroxylamine-mediated gold reduction (right). In the upper part of the panel, transmission electron micrographs (A, B) of nanoparticles and numerical size distributions (C, D) are reported. In the bottom part, XRD

spectrum of iron oxide nanoparticles (E) and the EDXA data referred to H-NPs (F) are

shown.

The results of TEM, XRD and EDXA analysis on hydrophobic nanoparticles

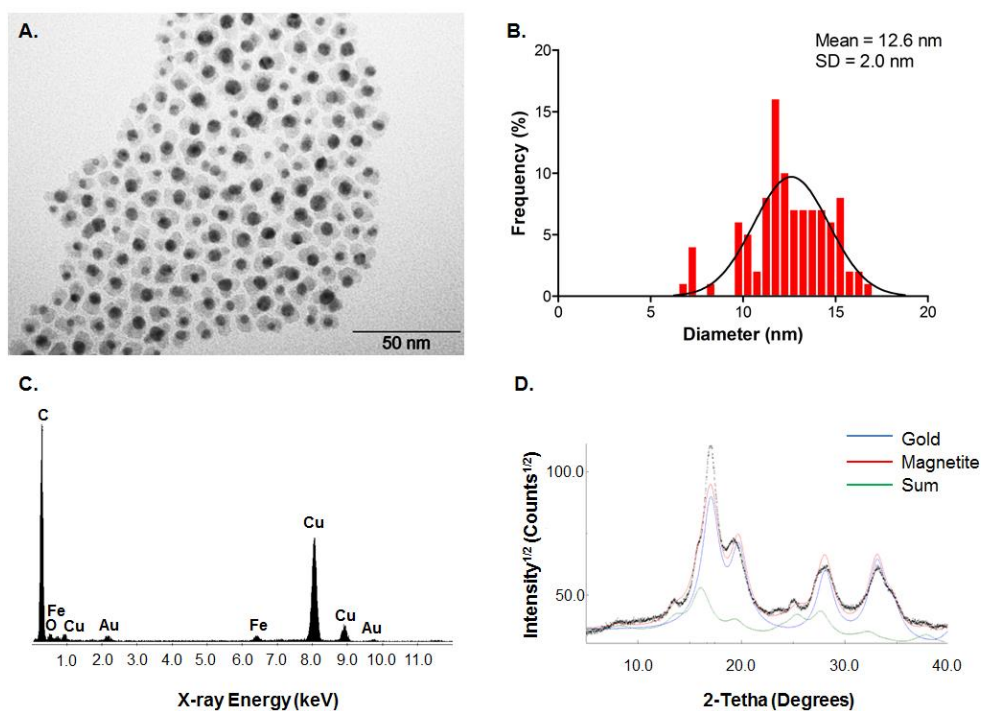produced by thermal decomposition of metal precursors are reported in Fig. 10.

Figure 10. Morphological and chemical characterization of hydrophobic H-NPs synthetized

by thermal decomposition. In the upper part, TEM image of nanoparticles (A) and numerical

size distribution (B) are reported. In the bottom part, EDXA results (C) and XRD spectrum

(D) of nanoparticles are shown.

TEM investigation highlights the formation of dumbbell-like nanostructures composed by a spherical gold part (the more contrasted one) and by an irregular iron oxide part (Fig. 10A). The hybrid nanostructures have an average diameter of 12.6 nm (Fig. 10B). EDXA analysis (Fig. 10C) confirmed the presence of gold and iron while XRD data assessed the iron oxidation in the form of magnetite (Fig. 10D). The data about the metal composition of nanoparticles synthetized by both methods are reported in Table 1.

	Batch	Gold (% wt.)	Iron (% wt.)	Others (% wt.)
Hydroxylamine-based method	#1	98.8	0.1	<0.1
Thermodecomposition-based method	#1	67.1	32.8	<0.1
	#2	60.9	39.0	<0.1

Table 1. Percent content of gold, iron and other metals in nanoparticles produced by hydroxylamine-based method and thermodecomposition-based method. The analysis was performed by ICP-OES on samples derived by different synthesis batches.

Negligible traces of metals different from gold and iron were detected in the samples confirming the absence of potentially dangerous residual metals after nanoparticle purification. The ICP-OES analysis of nanoparticles, produced by hydroxylamine-

based method, evidenced that nanoparticles are composed mainly by gold (98.8% wt.), while iron content is almost negligible. On the other side, nanoparticles, produced by thermodecomposition-based method, are composed by ~65% wt. gold and 35% wt. iron. Two different synthesis batches of those nanoparticles were produced and analysed providing similar results in terms of metal composition. Moreover, thermodecomposition synthesis method provided higher synthesis yield (~70% wt. metal precursors was transformed in nanoparticles) than the hydroxylamine-based methods.

Colloidal stability and hydrodynamic diameter of Tween20-capped dumbbell-like H-NPs was assessed in water and PBS solution by DLS. The results, reported in Fig. 11, highlight nanoparticles have a hydrodynamic diameter of ~30 nm and do not form aggregated either in water either in PBS.

Considering the impact that proteins could have on nanoparticles stability, the optical response of Tween20-capped dumbbell-like H-NPs incubated in MG63 cell culture medium was evaluated at different time-points. The UV-visible absorbance spectra of nanoparticles after 0h, 2h, 6h, 24h and 48h of incubation in cell culture medium are reported in Fig. 12. No changes in the optical absorption profile of nanoparticles occur over all the time-points and the profiles of nanoparticles in PBS and cell culture medium match well. In particular, no broadening or shift of the SPR

band occurs suggesting that Tween20 coating confers stealth properties to nanoparticles hindering nanoparticle agglomeration.
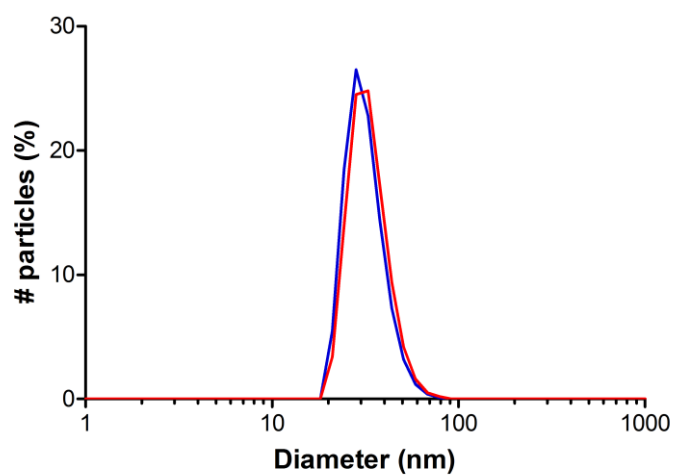

Figure 11. DLS analysis of Tween20-capped dumbbell-like H-NPs dispered in water (blue line) and PBS solution (red line).
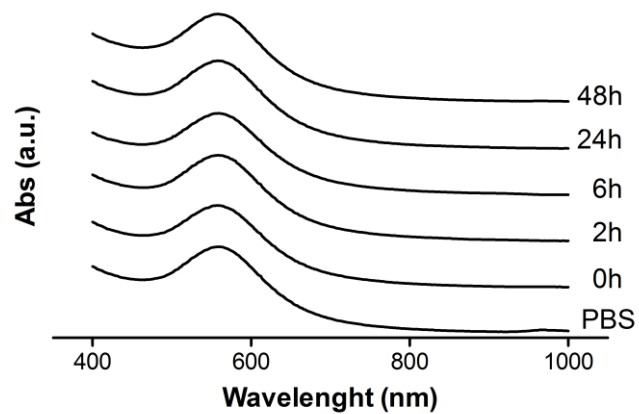
Figure 12. UV-visible absorption spectra of Tween20-capped dumbbell-like H-NPs at different time-points (0h, 2h, 6h, 24h and 48h) following incubation of nanoparticles in MG63 cell culture medium and PBS (0h). The spectra are nudged to allow a better visualization.

4.3.   Discussion

Hydrophilic gold-magnetite hybrid nanoparticles were synthetized by two synthesis methods. In particular, star-shape H-NPs were produced by a procedure involving the reduction of gold(III) chloride by hydroxylamine in presence of prefabricated iron oxide nanoparticles. Tween20-stabilized dumbbell-like H-NPs were synthetized by thermal decomposition of metal precursors in oil and transferred in water by Tween20 micelles. Nanoparticles produced by thermal decomposition method are smaller than nanoparticles produced by hydroxylamine-based method. In particular, the size of dumbbell-like H-NPs (12.6 nm) has been demonstrated to be better for nanoparticle-mediated radiosensitization[70]. Moreover, dumbbell-like H-NPs present a balanced gold and iron content (65% Au, 35% Fe), while star-shape H-NPs are composed by an extremely low iron amount (less than 1%). The poor iron content direct influences the magnetic properties and limits MR imaging potentialities.

In addition, Tween20-stabilized dumbbell-like H-NPs provide excellent colloidal stability in water and in physiological solution. Nanoparticles remained stable also in protein solution for up to two days confirming the efficacy of Tween20-capping in stabilizing nanoparticles, as expected by capping molecules composed by polyethylene glycol moieties.

As a consequence of the results so far presented, Tween20-capped dumbbell-like H-NPs were selected as candidates for MRI-guided radiosensitization and, in the

following dissertation, Tween20-stabilized dumbbell-like H-NPs will be named, simply, as H-NPs.

Chapter V

Study of the magnetic properties and the imaging potentialities of H-NPs

A fundamental issue in theranostic nanoparticles for radiotherapy enhancement regards the possibility to finely determine the biodistribution of nanoparticles following administration. In particular, the precise tracking of nanoparticle accumulation in cancer and surrounding tissues is expected to provide useful information to the physicians about the sensitization profile obtained in the target tissues allowing the optimization and the standardization of the dose delivery in radiotherapy.

Once injected in the blood, H-NPs are designed to be tracked by MR imaging exploiting the superparamagnetic properties of nanosized magnetite. Under an applied magnetic field, the magnetic momentum of superparamagnetic nanoparticles is aligned in the direction of the field inducing spatio-temporal inhomogeneities in the local magnetic field. Such inhomogeneities perturb the nuclear spin relaxation

process of H^1 protons of water molecules surrounding nanoparticles promoting the dephrasing of transverse proton spins. This effect results in the shortening of the spin-spin relaxation time (T2) and consequent darkening (negative contrast enhancement) of the T2-weighted MR image. Typically, MRI sequences for the acquisition of T2-weighted images are optimized to reduce as much as possible the dephasing effects of local magnetic inhomogeneities. When superparamagnetic contrast agents are used, the MRI signal arising from transverse magnetization of proton spins is acquired without any spin rephrasing expedient, using so-called T2*-weighted acquisition sequences.

The potentialities of H-NPs as contrast agents in MRI depend on their magnetic properties. In this section, the magnetic behaviour of H-NPs was assessed by the measurement of the magnetic hysteresis curve of nanoparticles and by the study of the influence of H-NPs on H^1 water proton spin-spin relaxation by nuclear magnetic resonance spectroscopy (NMR) investigations. The results were compared to literature values referred to other superparamagnetic nanoparticles for MR imaging. Furthermore, H-NPs were tested in a 4T-MRI whole-body scanner to investigate the dependency of imaging contrast enhancement to H-NP concentration using a typical T2*-weighted acquisition sequence.

5.1. Materials and methods

The magnetization curve of H-NPs was evaluated using an alternating gradient force magnetometer (AGFM) provided by the IMEM-CNR Center of Parma (Italy). The measurement was performed at room temperature.

The effect of H-NPs on the spin-spin relaxation time (T2) of H^1 water protons was investigated using a Bruker 400WB instrument, working at 400.13 MHz proton frequency. NMR spectra were acquired with single pulse, Car-Purcel-Meiboom-Gill echo train acquisition and inversion recovery sequences under the following conditions: 4.9 μs π/2 pulse, 10 s recycle delay, 8 scans. The T2 relaxation times of four nanoparticles samples at different iron molar concentrations (0, 0.125, 0.250, 0.500 mM) were calculated and the data were fitted in order to estimate the spin-spin relaxivity (r_2). Spin-spin relaxivity is defined by the equation $1/T2 = 1/T2^0 + r_2 \cdot [Fe]$, where $T2$ and $T2^0$ are the relaxation time of sample and pure water, respectively, and $[Fe]$ is the iron molar concentration of H-NPs.

A 4T-MRI Bruker Spec Med scanner, provided by MR Lab of the Center for Mind/Brain Sciences (University of Trento, Italy), was used to acquire the MRI-images of a phantom. The phantom consisted of a set of plastic tubes (syringes filled by 5 ml and sealed with impermeable tape) loaded with different concentrations of H-NPs (0.0, 1.7, 8.5, 17.0, 84.8 μg/ml). The array of tubes was positioned within a larger cylindrical recipient (25 cm height, 11 cm diameter), filled with water. The

whole phantom simulated biological tissues and kept the set of syringes positioned as a parallel array during the MRI acquisition (Fig. 13). Each syringe was carefully filled to minimize air bubbles that could affect the homogeneity of the magnetic field in the phantom. A standard anatomical T2*-weighted spin-echo sequence (TE = 44 ms, TR = 49 ms) was used to acquire the MR image of the phantom. Voxel size was 0.18 cm x 0.18 cm x 0.1 cm and 72 slices were acquired. The contrast enhancement provided by nanoparticles was evaluated in terms of the normalized brightness variation in function of the H-NP metal concentration. The H-NP concentration values are expressed in terms of total metal concentration ($C_{H-NPs} = C_{Au} + C_{Fe}$).
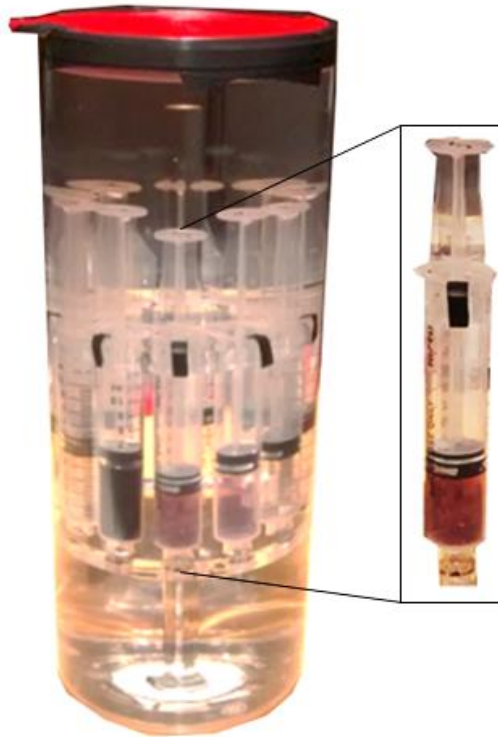
Figure 13. MRI phantom used in 4T-MRI scanner. Inside the phantom, a sample holder maintained the tubes parallel. In the box, a zoom of the plastic tube loaded with H-NP solution.

5.2. Results

The field-dependent magnetization curve of H-NPs is reported in Fig. 14A. At room temperature, negligible hysteresis is observed. This evidence is consistent with the hypothesis that nanoparticles are in the superparamagnetic state. The AGFM measurement shows saturation magnetization value of ~35 emu per gram of iron saturation magnetization value and coercivity value of ~15 kOe. As expected from superparamagnetic nanoparticles, the relaxation rate (1/T2) of H^1 water protons increased by increasing the concentration of H-NPs. The NMR data are shown in Fig 14B and, as result of linear regression analysis, 156.4 mM^{-1}s^{-1} *r2* value was obtained. These results compare well with previously reported literature values[88–90].
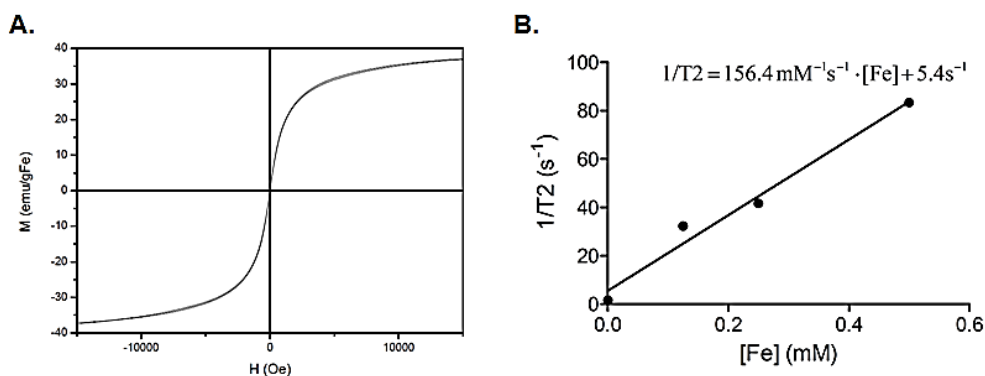

Figure 14. Magnetization curve of H-NPs measured at room temperature (A) and transverse relaxation rates (1/T2) vs. Fe concentration measured at 9.4 T.

The contrast enhancement of H-NPs was investigated using a 4T-MRI whole-body scanner. A T2*-weighted image of a phantom loaded with samples at different nanoparticle concentrations was acquired. In Fig 15A, the MRI-images of a transverse section of the samples are shown. In Fig 15B, the normalized brightness of the samples is plotted in function of nanoparticle concentration. The trend follows an exponential decay of the normalized brightness versus nanoparticle concentration. Under those acquisition parameters, a detection limit of approximately 8 μg/ml H-NPs was estimated.
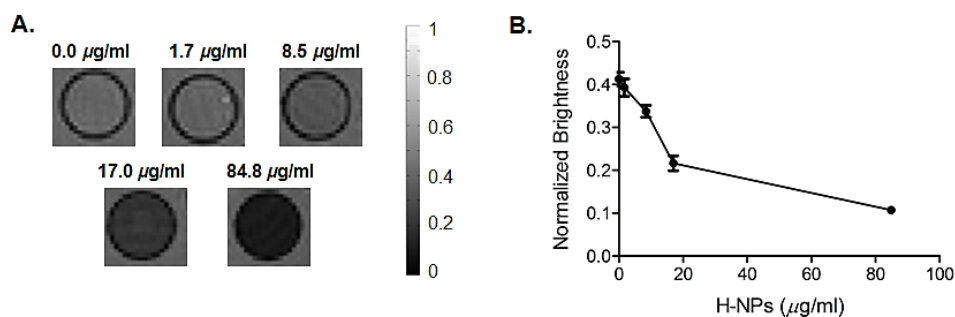

Figure 15. T2*-weighted MR image of a transverse section of H-NP samples (A). The grayscale defines the normalized brightness. Average and SD normalized brightness of the imaging area referred to each sample are reported in function of H-NP concentration.

5.3. Discussion

The magnetic properties of gold-magnetite hybrid nanoparticles synthetized by thermal decomposition method and stabilized in water by Tween20 micelles were studied. The results highlighted that H-NPs are in the superparamagnetic state at room temperature with magnetization saturation value and coercivity value consistent with the values previously reported in literature for superparamagnetic nanoparticles. The influence of water-dispersed H-NPs on the spin-spin relaxation of H1 water protons was studied by NMR spectroscopy. The measurement provided a value of *r2* relaxivity similar to the typical relaxivity values of previous reported magnetite nanoparticles for MR-contrast imaging. Finally, H-NPs were tested in a real-case configuration using a whole-body 4T-MRI scanner showing an exponential decay trend between the contrast enhancement in the T2*-image and the H-NP concentrations in the examined samples. Approximately 8 ug/ml H-NPs was estimated as the minimum detectable H-NP concentration. The detection limit of H-NPs is similar to that of gadolinium nanoparticles in T1-weighted images as reported by Le Duc et al confirming H-NPs provide imaging potentialities comparable to those offered by gadolinium nanostructures[74].

Chapter VI

Biological evaluations

Gold-magnetite hybrid nanoparticles could potentially provide relevant advances in a wide range of oncologic diseases. In particular, H-NPs are expected to successfully operate as MRI-contrasted radiotherapy adjuvants in case of solid cancers with certain anatomical and physiological features, including defective blood vessel architecture (enhanced permeability and retention effect) and radioresistance.

Osteosarcoma, an aggressive solid bone cancer with an incidence rate of approximately 5.0 per year per million persons for the range 0-19 years[91], represents an optimal candidate for the implementation of theranostic H-NPs. In fact, previous *in vivo* studies regarding curcumin liposomes and polymer nanoparticles for osteosarcoma care revealed that osteosarcoma can be effectively targeted by nanoparticles through passive targeting[92,93]. In addition, osteosarcoma cells are known to be particularly radioresistant, limiting the use of radiotherapy in lesions occurring in the extremities, the base of skull, the pelvis and the neck, where

satisfactory surgical resection is difficult to achieve with acceptable margins[94]. Successful osteosarcoma radiotherapy requires high radiation dose delivery with consequent risk of adverse events in the surrounding healthy tissues[95,96]. In this scenario, theranostic H-NPs could provide osteosarcoma radiosensitization enabling precise dose shaping and optimal radiotherapy timing by real-time MRI-tracking of nanoparticle distribution in the cancer lesion.

In this section, the potentialities of H-NPs for osteosarcoma radiosensitization are investigated *in vitro* using human osteosarcoma MG63 cells. In addition, parallel biological evaluations were conducted on murine embryonic fibroblast 3T3 healthy cells in order to estimate possible drawbacks related to H-NPs utilization. In fact, osteosarcoma radiotherapy is often followed by orthopedic surgery for cancer resection and fibroblasts play a fundamental role in the first stages of bone healing, as they are a source of osteoblast precursors. Therefore, any osteosarcoma treatment should prevent as much as possible any damages to fibroblast population in order to reduce the recovery time following osteosarcoma resection.

Biological assays were performed on MG63 cells and 3T3 cells in order to estimate potential cytotoxicity of H-NPs at nanoparticle concentrations typically used in medical applications. Cytotoxicity was evaluated in terms of cell membrane integrity and cell morphology changes following incubation with cell media loaded with nanoparticles. Cell membrane integrity was measured by lactase dehydrogenase

(LDH) assay that estimates the amount of cytoplasmic lactase dehydrogenase enzyme released in the culture supernatant as result of cell apoptosis or necrosis. Cell morphology was investigated by laser scanning confocal microscopy on nanoparticle-exposed cell cultures, stained with cytoskeleton-specific and nuclei-specific fluorescent dyes. Confocal microscopy was also used to assess the intracellular distribution of fluorescence-labelled nanoparticles allowing considerations about the internalization processes occurring in cellular uptake of nanoparticles. The potentialities of H-NPs for cellular radiosensitization were evaluated by viability assay performed on clonogenic cell cultures, incubated with nanoparticles and treated with megavoltage radiotherapy. Due to the lag time between the irradiation and the occurrence of radiation damages in the cells, clonogenic assays are commonly used in radiobiology as they provide a reliable estimation of long-term effects of radiations in cell cultures. In radiobiological clonogenic assays, cells are irradiated and reseeded using low cell density. Then, cell viability is estimated after some days from the irradiation. In our experiment, alamar blue kit assay was used to measure clonogenic cell viability after five days from irradiation. In particular, alamar blue allowed the determination of cellular metabolic activity in the clonogenic cultures. Although metabolic activity assays are not the standard goal for radiobiological clonogenic experiments, a previous study of Anoopkumar-Dukie et al demonstrated that the results of alamar blue-like assays

are consistent with convectional assays for the estimation of cell surviving fraction and cell proliferation, including microscope counting of stained cells or other assays aimed to measure the synthesis rate of new DNA in cell cultures[97]. The results are briefly discussed to evaluate the potential implementation of H-NPs in the clinical management of osteosarcoma.

6.1. Materials and methods

Cell cultures

Human bone osteosarcoma MG63 cells and immortalized mouse embryonic fibroblast 3T3 healthy cells were employed for the *in vitro* tests. MG63 cells were cultured using MEM, supplemented with 10% fetal calf serum, 1% sodium pyruvate, 1% MEM NEAA 100x, 1% L-glutamine and 1% penicillin–streptomycin. 3T3 cells were cultured using DMEM supplemented with 10% fetal calf serum, 1% sodium pyruvate, 1% L-glutamine and 1% penicillin-streptomycin. Cell cultures were maintained in humidity-controlled incubator at 37°C and 5% CO_2.

Lactase dehydrogenase assay

LDH in vitro assay (Kit TOX7, Sigma-Aldrich) was used to evaluate the short-term cytotoxicity of H-NPs. The kit allows the quantification in the cell culture supernatant of lactate dehydrogenase (LDH), a cytoplasmic enzyme used as marker of cell integrity. LDH enzyme is released by cells in case of damage to the cell membrane. To perform the LDH assay, 2×10^4 cells/cm^2 was seeded and, after 24h, cells were exposed for 48h to culture media loaded with H-NPs at nanoparticle concentrations of 10 μg/ml, 50 μl/ml and 100 μg/ml. The H-NP concentration values are expressed in terms of total metal concentration ($C_{H-NPs} = C_{Au} + C_{Fe}$). The concentration values were chosen according to previous studies about *in vitro* tests of hybrid

nanoparticle[89,98]. The LDH test was performed following the manufacturer's instructions. Negative (cells cultured in normal conditions) and positive (complete loss of membrane integrity) controls were used to test the assay robustness. Cells cultured with nanoparticle-free medium were used as negative controls. Cells incubated with culture medium loaded with 0.5% w/v Triton-X, a non-ionic surfactant able to permeabilize cell membrane, were used as positive controls.

Confocal laser scanning microscopy

Cell morphology and cellular internalization of nanoparticles following H-NP incubation were evaluated by laser scanning confocal microscopy, using a Nikon Eclipse Ti-E system. H-NPs were preliminary stained with DiI (1,1'-didodecyl-3,3,3',3'-tetramethylindocarbocyanine perchlorate, Invitrogen), a hydrophobic dye suitable for fluorescence labelling of nanoparticles. In particular, DiI molecules are embedded in H-NPs and segregated at the hydrophobic interface among the metal surface and the lauric acid moities of Tween20 molecules. The staining process was carried out as suggested by Landazuri et al[99]: H-NPs were incubated overnight with 20 μg/ml DiI solution and washed by centrifugation. Then, 2×10^4 cells/cm^2 were seeded on 8-wells glass chamber slide (Thermo Scientific, USA) and, after one day from the seeding, they were exposed for 24h to culture medium loaded with 100 μg/ml DiI-stained H-NPs. Cells were washed several time with PBS, fixed with 4%

formaldehyde and permeabilized with Triton-X (0.2% w/v in PBS). 4',6-diamino-2-phenylindole DAPI (Sigma-Aldrich) and Oregon Green® 448 phalloidin (Invitrogen, Life Technologies) were used to stain the nuclei and the cytoskeleton actin filaments, respectively.

Alamar blue assay

A clonogenic assay was performed to evaluate the radiosensitizing potentialities of H-NPs in MG63 and 3T3 cell cultures. 8×10^4 cells/well was seeded in a 12-well-tissue culture plate. After 24h from the seeding, the medium was removed and fresh medium, loaded with H-NPs at different concentrations (0 μg/ml, 1 μg/ml, 10 μg/ml, 100 μg/ml), was added. Following 24h exposure to NP-loaded medium, cell cultures were transferred to the Radiotherapy Department of Santa Chiara Hospital (Trento, Italy) for the irradiation. An Elekta Precise Treatment System equipment was used to irradiate cells with 10 Gy radiation dose, 6 MVp peak energy. A radiation field of 20x20 cm was used. The electronic equilibrium in the cell cultures was ensured by placing cell culture plates into a properly designed phantom as shown in Fig 16.

Figure 16. Experimental set up used for the irradiation of cell cultures. In the box, the plexiglas phantom used to ensure the electronic equilibrium in cell cultures during the irradiation.

Immediately after irradiation, the medium was removed and cells were detached by Trypsin 0.05% w/v, counted and reseeded in 48-well tissue-culture plates using fresh NP-free medium. Considering the different proliferation rate of MG63 cells and 3T3 cells, two seeding densities were used depending on the cell type. In particular, 5×10^3 cells/well and 5×10^2 cells/well seeding density were used for MG63 cells and for 3T3 cells, respectively. At day 3 after reseeding, the medium was removed and fresh medium was added. At day 5, cell viability was assessed by alamar blue kit assay (Biosource International, USA), following the manufacturer's instructions. Alamar blue assay is based on the ability of viable and metabolically active cells to reduce resazurin by mitochondrial, microsomal and cytosolic oxidoreductases. The

reduction of resuzin results in the formation of resorufin, a fluorimetrically measurable compound.

Statistical analysis

All values are listed as mean and standard deviation (SD). Statistical analysis was performed on the LDH and alamar blue results. In the case of alamar blue, the group sets referred to 0 Gy-treated and 10 Gy-treated samples were analysed separately. Unpaired t-test with equal variances, adjusted by Bonferroni correction, was used with a 0.05 significance level.

6.2. Results

Membrane integrity of MG63 cells and 3T3 cells after 48h exposure to different concentrations of H-NPs was tested using lactate dehydrogenase (LDH) assay. The LDH data are reported in Fig. 17 and are directly proportional to the number of dead cells. No significant differences in LDH leakage into the media was detected over all the range of nanoparticle concentrations and the negative control either for MG63 cells and 3T3 cells. The results were consistent to previous studies regarding cytotoxicity induced by iron oxide and gold nanoparticles[20]. In particular, the LDH assay confirmed that no unsafe contaminations occurred in the synthesis of nanoparticles, although Tween20 had been discovered to induce moderated cytotoxicity[100].

The study of the cellular uptake process was conducted by confocal laser scanning microscopy on MG63 cells and 3T3 cells using DiI-labelled H-NPs. Following 24h incubation, H-NPs are taken up either by MG63 cells and 3T3 cells as shown by confocal laser images, reported in Fig. 18 and Fig. 19. In particular, internalized nanoparticles appeared clustered in localized intracellular compartments. This evidence is consistent to previous studies that identified lysosomes as the preferential accumulation sites for nanoparticles taken up by pinocytosis mechanism[101]. The comparison among confocal images of cells exposed to

nanoparticles and the controls did not reveal remarkable changes in cell morphology indicating H-NP safety.

The synergetic effect of H-NPs and megavoltage radiations on cell viability was evaluated by alamar blue assay on clonogenic MG63 and 3T3 cell cultures exposed to different concentrations of H-NPs and irradiated with 10 Gy radiation dose (6 MVp). The results, reported in Fig. 20, highlight nanoparticles alone do not affect cell viability either in MG63 and 3T3 cells confirming that H-NPs as well are safe. The comparison between the group sets referred to RT-treated samples and the not-treated ones reveals that radiotherapy induced a dramatically decrease of cell viability in all samples. Approximately 20% and 28% reduction of MG63 cell viability occurred in RT-treated samples incubated with H-NP-loaded media, respectively at 10 µg/ml and 100 µg/ml nanoparticle concentration, compared to RT-treated samples cultured in NP-free medium. This evidence supports the hypothesis that H-NPs enhance radiation toxicity in osteosarcoma cells. On the contrary, no significant differences were detected in 3T3 cell cultures treated with nanoparticles and radiations versus cells treated with radiotherapy only, indicating H-NPs do not induce radiosensitivity enhancement in fibroblast cells. The statistical difference in RT-treated cells incubated with 1 μg/mg nanoparticles versus cells treated with RT only is probably due to an error in the number of cells reseeded after radiotherapy.
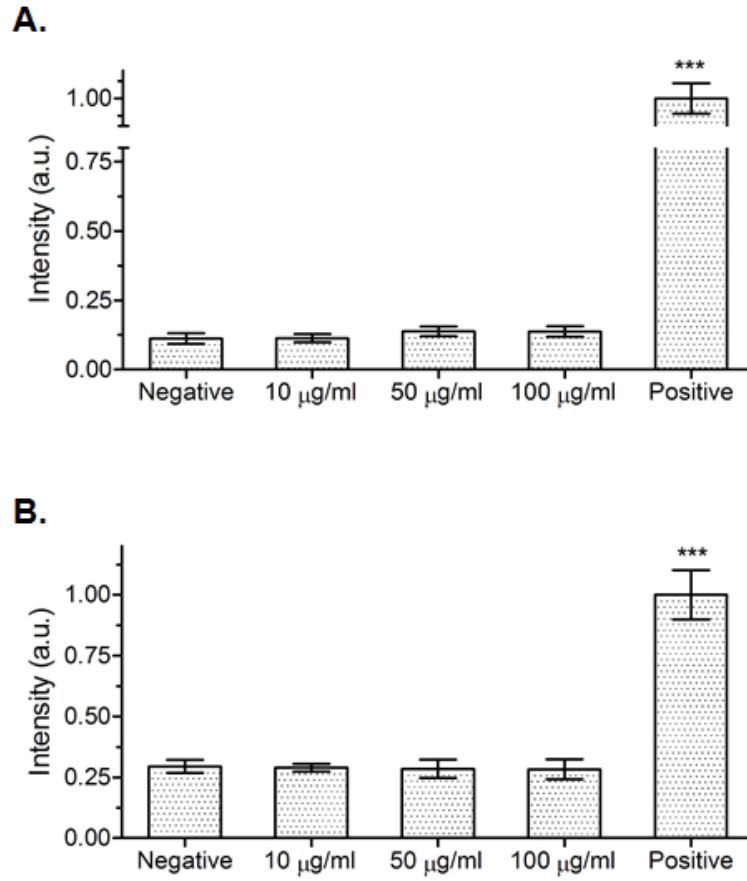
Figure 17. LDH assay performed on MG63 cell line (A) and 3T3 cell line (B). Negative and positive control consisted of cells cultured with NP-free medium and with Triton-X-enriched medium, respectively. ($n=6$). ***$p<0.001$ versus the negative control.
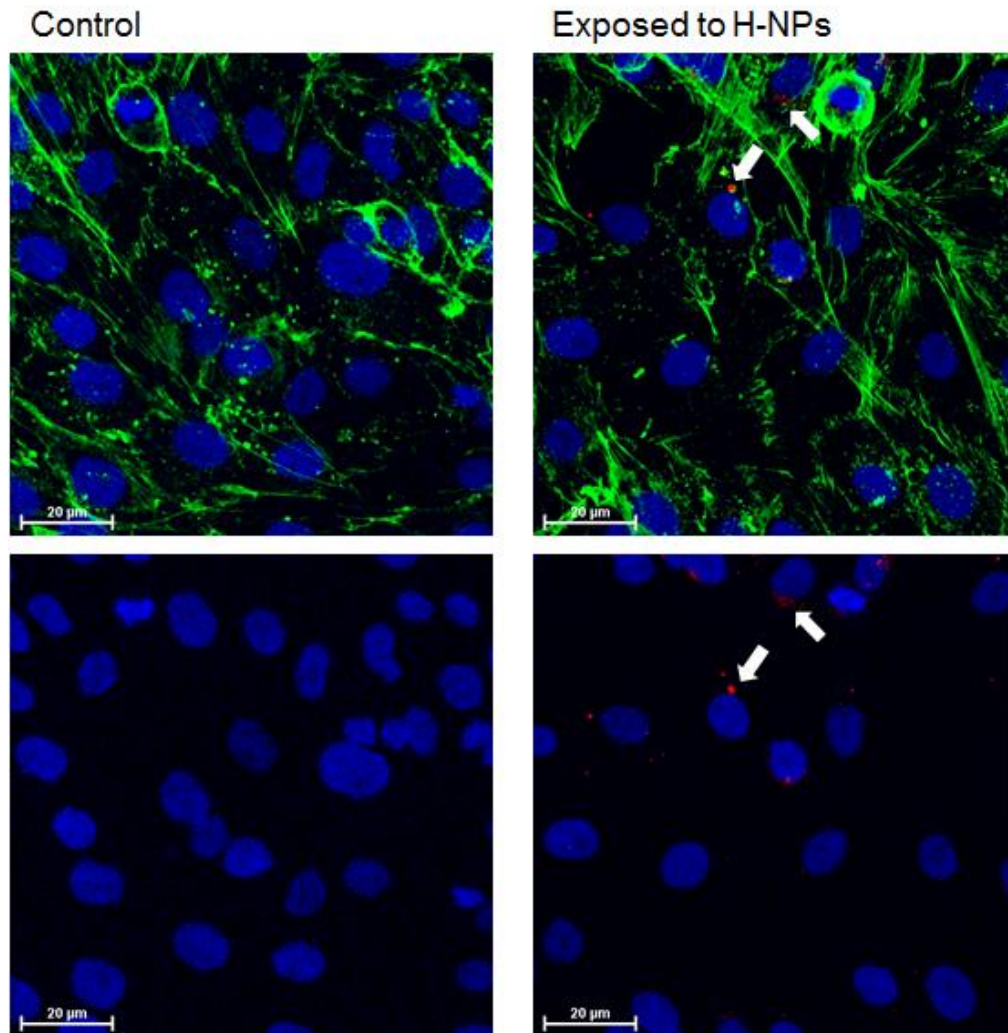
MG63 cell line

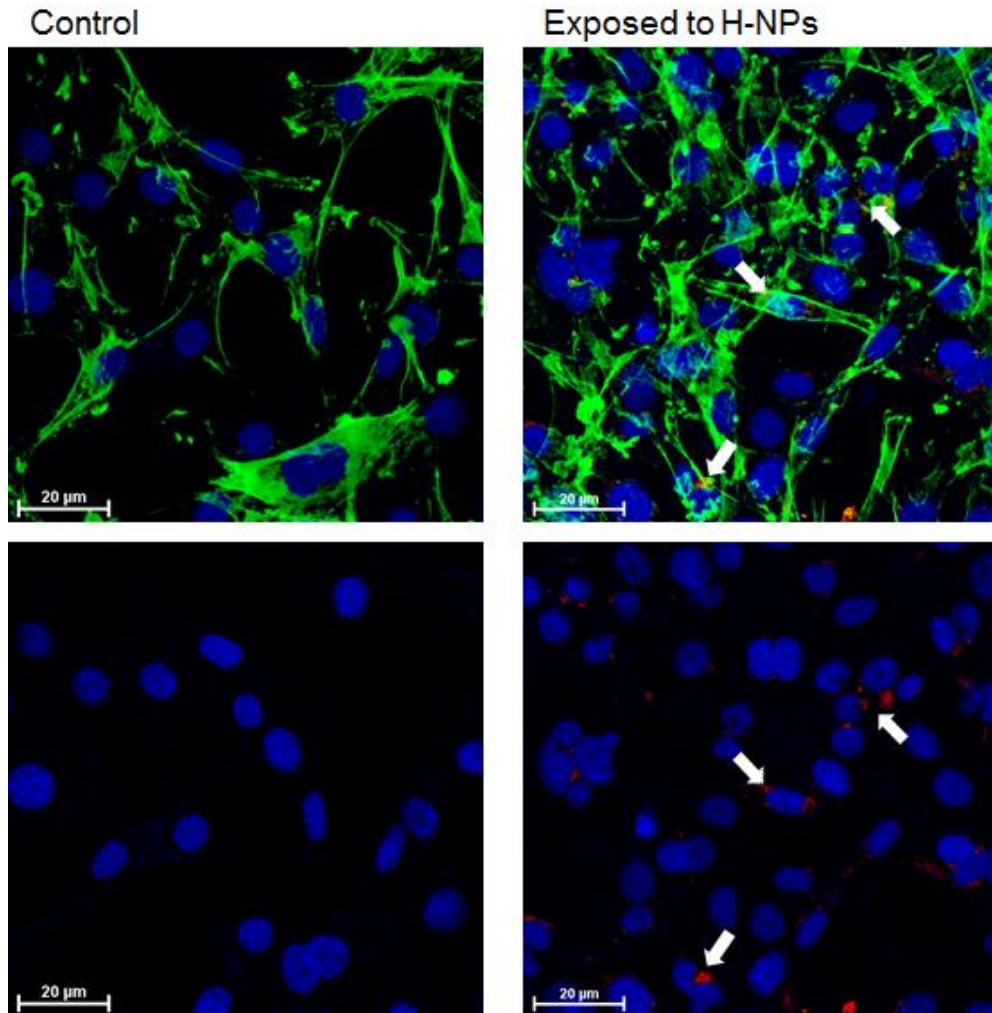Control　　　　　　　　　　　Exposed to H-NPs

Figure 18. Confocal laser scanning microscopy of MG63 cells cultured with NP-free medium (on the left) and 24h exposed to NP-loaded medium (on the right). Cells were stained with DAPI (blue) and Oregon Green (green), while H-NPs were stained by DiI (red). On the bottom part, the images are reported without Oregon Green staining. The arrows indicate the presence of H-NPs.

Figure 19. Confocal laser scanning microscopy of 3T3 cells cultured with NP-free medium (on the left) and 24h exposed to NP-loaded medium (on the right). Cells were stained with DAPI (blue) and Oregon Green (green), while H-NPs were stained by DiI (red). On the bottom part, the images are reported without Oregon Green staining. The arrows indicate the presence of H-NPs.
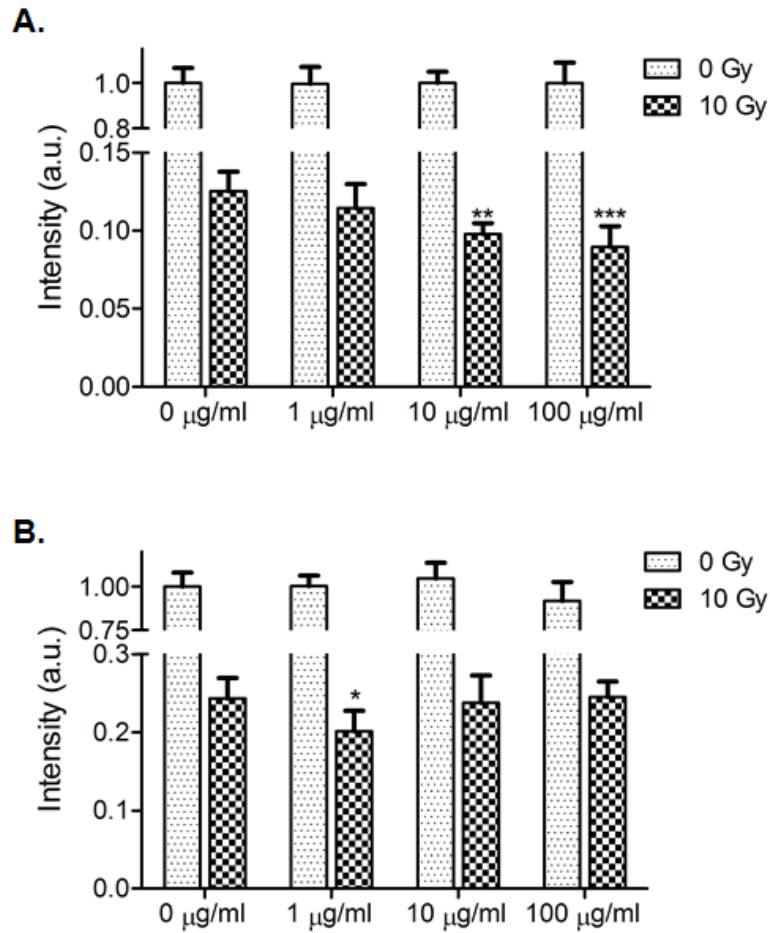
Figure 20. Alamar blue performed on MG63 cells (A) and 3T3 (B) following 24h exposure to NP-loaded medium at different H-NP concentration (0, 1, 10, 100 μg/ml), treated with 0 Gy and 10 Gy radiation dose. (n=6). *p<0.05, **p<0.01, ***p<0.001 versus 0 μg/ml group treated with 10 Gy.

6.3. Discussion

The biological assays performed on MG63 cells and 3T3 cells confirmed that H-NPs do not induce cytotoxicity in both cell lines examined in this study. In particular, LDH assay, confocal laser scanning microscopy and alamar blue assay revealed no change in membrane integrity and morphology following nanoparticles exposure, even for high nanoparticle concentration (100 μg/ml). The results were consistent to previous cytotoxicity studies of gold and iron oxide nanoparticles[20]. In addition, confocal laser scanning microscopy assessed the internalization of fluorescence-labelled H-NPs and the evidence of nanoparticle segregation in specific cellular compartments suggests that pinocytosis could be the main mechanism occurring in the uptake process.

The potentialities of H-NPs for radiosensitization were investigated by the measurement of cell viability in clonogenic MG63 and 3T3 cell cultures exposed to H-NPs and irradiated by 10 Gy radiation dose. No synergetic effect of H-NPs and radiations was highlighted in fibroblast cell line while approximately 20% and 28% reduction of cell viability was estimated in radiotherapy-treated osteosarcoma cell cultures incubated with 10 µg/ml and 100 µg/ml nanoparticle concentrations compared to cell cultures treated with radiotherapy only. Therefore, a selective radiosensitization activity of H-NPs was demonstrated to occur in osteosarcoma cells, although the mechanisms of such selectivity are still not clear and more

studies are required for a deep understanding of the sensitization process. The results of radiobiological assay, although very preliminary, confirmed the potentialities of H-NPs for osteosarcoma radiotherapy. In fact, H-NPs were proven to enhance the outcomes of radiotherapy in osteosarcoma cells without affecting a fundamental resource for post-surgery recovery. However, convectional radiobiological assays, based on the estimation of cell proliferation and survival after irradiation, are needed to confirm the results of our metabolic activity assay.

As reported in literature, other cell types are well sensitized by gold nanoparticles. For instance, cell lines derived from prostate, breast and cervical cancers have been experience high radiosensitization if cultured in gold nanoparticle-enriched media[68–70]. Thus, beside osteosarcoma, H-NPs claim to be a successful tool for the radiosensitization of a wide range of cancer types.

Chapter VII

Conclusions

Theranostics defines a class of medical methods based on the use of therapeutic agents able to test the patient's response to the therapy, allowing treatment modulation and personalization. Recently, nanoparticles have been identified as promising platforms for cancer theranostics, thanks to their peculiar biological mobility and physico-chemical properties. In particular, properly designed nanoparticles have been proven to selectively target solid cancers as the defective architecture of tumour blood vessels allows the extravasation and retention of nanoparticles in the cancer (EPR effect), while normal tissues are generally preserved from nanoparticle accumulation.

In this work, gold-magnetite hybrid nanoparticles (H-NPs) are proposed as innovative theranostic tools for imaging-guided radiosensitization. The biphasic structure of H-NPs combines the potentialities of superparamagnetic magnetite nanoparticles for MR imaging and the radiosensitization performances of gold nanoparticles in a unique nanoplatform. The imaging power of magnetite

nanoparticles is well-known and arises from the ability of superparamagnetic nanoparticles to induce contrast enhancement in T2*-weighted MR images. On the other hand, gold nanoparticles are efficient x-ray absorber and, once internalized in cells, induce concentration-dependent radiosensitization by enhancing local deposition of radiation dose. The combination of imaging and radiosensitization offered by H-NPs should allow the implementation of effective theranostic radiosensitization. In particular, the biodistribution of blood-injected H-NPs is trackable by MR imaging, providing a real-time picture of the radiosensitivity profile across the tumour lesion. The imaging data can be used to determine the optimal time-point and radiation shape in radiotherapy, allowing a significant reduction of the radiation dose required for cancer local control in comparison to standard radiotherapy. Theoretically, H-NPs are expected to perform better than convectional low-molecular-weight radiosensitizers and other theranostic nanoparticles, like gold and gadolinium nanoparticles. In particular, compared to molecular drugs, H-NPs should offer higher radiosensitization performances and the opportunity for treatment personalization. Furthermore, H-NPs are expected to overcome the limitations imposed by gold nanoparticles and gadolinium nanoparticles in terms of safety concerns due to CT imaging and poor radiosensitization, respectively.

The experimental work was set up to address the following aims:

i)   to synthetize H-NPs able to match the requirements of size, chemical composition, colloidal stability, and magnetic properties highlighted by previous studies about medical nanoparticle for MR imaging and radiosensitization.

ii)   to deliver preliminary in vitro evaluations about biosafety, imaging potentialities, radiosensitizing performances of H-NPs using clinical MRI scanner and osteosarcoma-model cell lines.

Two innovative synthesis methods have been tested to achieve H-NPs suitable for our purposes. The first method involved gold reduction on prefabricated magnetite nanoparticles by hydroxylamine in aqueous environment (hydroxylamine-based method). The process provided star-shaped H-NPs with average diameter of ~63 nm and metal content of 98.8% wt. gold and ~0.1% wt. iron. The extremely low amount of iron was though to result in poor MR imaging potentialities. In addition, the size of the nanoparticles exceeds the requirement for effective nanoparticle-mediated radiosensitization[70]. Therefore, hydroxylamine-based method was discharged as potential synthesis method for the production of reliable theranostic nanoparticles, although star-shape hybrid nanoparticles might result suitable for other biomedical applications (e.g. magnetic sorting, biosensing).

The second synthesis process was based on a two-steps method based on the synthesis of oil-soluble hybrid nanoparticles by thermal decomposition of metal precursors and the further oil-to-water transfer of nanoparticles by Tween20 micelles (thermodecomposition-based method). Tween20 is a surfactant with polyethylene glycol hydrophilic moieties that was used in the past for the stabilization in water of hydrophilic nanoparticles for medical applications. Here, Tween20 was tested for the first time to stabilize hydrophobic hybrid nanoparticles. The process allowed the production of hydrophilic dumbbell-like H-NPs with average diameter of ~12 nm and 65% wt. gold and 35% iron metal content. The chemical characterization confirmed thermodecompostion-based process provides good reproducibility over different synthesis batches and acceptable yield. Moreover, the resulting nanoparticles maintained colloidal stability in saline and protein solution at physiological conditions for a time interval typically required for medical applications (more than two days). The study of magnetic properties confirmed H-NPs, synthetized by thermodecomposition-based method, are in the superparamagnetic state with coercivity, magnetization saturation and T2-relaxivity values consistent with previously reported magnetite-based nanoparticles designed for medical applications. Therefore, Tween20-stabilized dumbbell-like H-NPs were identified as potential candidate for MRI-guided radiosensitization and then tested in human 4T-MRI scanner and *in vitro* cell culture experiments.

The biological evaluations of H-NPs were conducted on human osteosarcoma MG63 and murine fibroblast 3T3 cell cultures. The results revealed that no cytotoxicity occurred in both cell cultures following exposure to H-NPs, even at high nanoparticle concentration (100 μg/ml). In particular, nanoparticles do not affect membrane integrity and morphology of cells and pinocytosis was proposed as the main uptake mechanism occurring in the internalization process of nanoparticle in cells. A clonogenic assay was conducted to study the radiosensitizing activity of H-NPs through the quantification of the metabolic activity of cell cultures after exposure to nanoparticles and to 10 Gy megavoltage radiations. The results assessed that H-NPs induce selective radiosensitization of osteosarcoma cells. In particular, irradiated osteosarcoma cells incubated with 10 μg/ml and 100 μg/ml H-NP-loaded media were respectively 20% and 28% less viable than irradiated cells without H-NPs. On the other side, no synergic effect of radiations and nanoparticles was found in fibroblasts. Considering the fundamental role of fibroblasts in the recovery process following post-irradiation surgery, the evidence of osteosarcoma-specific radiosensitization provides a preliminary confirmation about the suitability of H-NPs for clinical implementation in osteosarcoma radiotherapy. Another confirmation arises from the evaluation of the theranostic potentialities of H-NPs. In particular, the analysis of the imaging performances of nanoparticles revealed that MR imaging provides reliable nanoparticle tracking in the range of concentrations effective of

radiosensitization. This evidence matches the basic requirement of theranostics, namely that the imaging window for the detection of the theranostic agent matches the concentration range with significant therapeutic efficacy.

The experimental achievements addressed in this work provide innovative findings in the field of nano-theranostics based on gold-magnetite hybrid nanoparticles. A novel method for the production of blood-injectable Tween20-stabilized dumbbell-like gold-magnetite hybrid nanoparticles with morphological, chemical and magnetic characteristics suitable for cancer targeting and MR imaging was set up. In particular, Tween20 was identified as a reliable alternative to more expensive capping agents for the water stabilization of hydrophobic hybrid nanoparticles[89]. Tween20-stabilized H-NPs were proposed as novel theranostic tools for MRI-guided radiosensitization of osteosarcoma cancer. In particular, H-NPs were proven to provide concentration-dependent osteosarcoma-specific radiosensitization in the concentration range suitable for MRI-tracking of nanoparticle distribution. However, our results are still preliminary and more studies are required to confirm the radiosensitization activity of H-NPs by convectional radiobiological assays and to investigate the mechanisms at the base of the osteosarcoma-specific radiosensitization. In addition, *in vivo* studies are strongly demanded to evaluate the capability of H-NPs to deliver theranostic radiosensitization in more realistic models.

Furthermore, the potentialities of H-NPs may be expanded in other cancer types. In fact, previous studies demonstrated that prostate, breast and cervical cancer cells respond well to gold nanoparticle radiosensitization, suggesting that H-NPs may provide theranostic radiosensitization in several cancer types. An extensive experimental campaign is therefore requested in order to identify new biological targets for potential H-NP implementation.

Appendix

Study of the role of size and surface chemistry of gold nanoparticles on blood protein adsorption

During the PhD activity, a preliminary study was conducted in order to investigate the role of size and surface chemistry of gold nanoparticles on the process of blood protein adsorption on the nanoparticle surface. The understanding of the influence of nanoparticle size and surface functionalization in the protein opsonozation is fundamental for the design of medical nanoparticles with favourable biological interactions in the blood tissue, as previously discussed in Chapter 1.2. In this work, we investigated the interactions between plasma proteins and gold nanoparticles (AuNP) developing ad hoc protocols to study the role of surface curvature and chemistry. AuNP with different size (10, 60 and 200 nm diameter) and surface chemistry (citrate and polyethylene glycol [PEG]) were analyzed. Citrate-coated AuNP are named 10 cAuNP, 60-cAuNP and 200-cAuNP depending on the size,

while PEG-coated nanoparticles are labelled as10-pAuNP, 60-pAuNP and 200-pAuNP. PEG was selected as coating due to its anti-fouling properties.

To emphasize the effect of curvature and surface reactivity of gold materials, we compared AuNP to gold macroscopic surface. Bare and PEGylated gold laminae were prepared and used as macroscopic control.

The characterization of AuNP was performed through scanning electron microscopy (SEM) and dynamic light scattering (DLS), while laminae were characterized using X-ray photoelectron spectroscope (XPS).

The effect of size and surface chemistry on the hydrodynamic radius of nanoparticles following incubation in human serum albumin and platelet-poor plama (PPP) solutions was evaluated by dynamic light scattering measurements.

Different elution media, including sodium dodecyl sulfate (SDS), urea and sodium hydroxide in isopropyl alcohol (isopropyl alcohol:NaOH), were used to desorb proteins from AuNP and their elution efficacy was tested.

Then, we focused on the comparison between protein adsorption on the different gold material following incubation with platelet-poor plasma to study the differences in composition of the protein corona at the equilibrium.

Material and methods

Gold materials

Citrate-coated gold nanoparticles (cAuNP) were purchased from TedPella (Redding, California). As reported by the manufacturer, a citrate shell surrounds nanoparticles to avoid aggregation by electrostatic repulsion. Thiolate-terminated PEG (3,500 Da, Sigma-Aldrich) was used to produce PEGylated gold nanoparticles (pAuNP) by incubating overnight cAuNP with solution containing a number of PEG moles equivalent to the moles of gold atoms on the surface of AuNP.

AuNP were characterized by SEM imaging (FE-SEM Supra 40, Zeiss) using an InLens detector at 2–4 kV acceleration voltage. The hydrodynamic radius of AuNP was evaluated by DLS (Zetasizer 1000, Malvern). The planar gold samples consisted of gold films deposited on silicon substrate chips with a surface area of 1.5 cm x1.0 cm. The chips were incubated for 10 min in piranha solution (1/3 hydrogen peroxide and 2/3 sulfuric acid), then immersed in boiling water and slowly cooled down to room temperature. Ethanol was used to wash quickly the surfaces, which were then treated by RF oxygen plasma (15 s at 200 W). After plasma treatment, bare surfaces were stored in ultrapure isopropyl alcohol, while PEGylated surfaces were incubated overnight with thiolated PEG solution (1 mM in ethanol 96 % vol.). Chemical surface characterization was performed using an ESCA200 instrument (Scienta-Gammadata ESCA200Uppsala Sweden).

Size of protein–AuNP complex

The effects on size of AuNP after incubation with plasma proteins were studied using a protocol that involved incubation of nanoparticles with protein solutions, removal of unbound proteins and analysis of nanoparticle size distribution. 45 µg of AuNP were suspended in 1.5 ml protein solution, including PPP at physiological concentration and HSA (1.0 mg/ml), and incubated for 15 min at 37°C. The samples were then centrifuged 30 min at 8,950 g, resuspended in PBS buffer solution and washed twice (30 min at 8950 g). Size distributions of AuNP after protein adsorption were acquired using DLS.

Protein desorption test

Different media to desorb proteins from AuNP surface were tested: SDS 0.1 % w/v, 8 M urea, and isopropyl alcohol:NaOH (2:3; isopropyl alcohol 99.5 %: 50 mM sodium hydroxide). PBS was used as negative control. Three replica for each type of eluting buffer were used. To remove residual unbound proteins from the suspension, four washing steps (30 min centrifugation at 10,000 g in PBS buffer solution) were applied. Then samples underwent the desorption process by incubation (1 h at 37°C) with 500 µl SDS (0.1 % w/v), 8 M urea, isopropyl alcohol:NaOH and PBS, respectively. After that, samples were washed (30 min centrifugation at 10,000 g), AuNP pellets were collected and supernatants were

lyophilized. Residual AuNP pellets and desorbed protein samples were suspended in sodium borate buffer (pH 9.3) and analyzed using a sensitive kit for protein quantification (CBQCA, Invitrogen).

Protein adsorption profiles

A specific protocol was developed to compare the protein adsorption profiles of the different gold materials (AuNP and laminae).

The procedure included: (i) incubation of gold materials with PPP solution at physiological concentration; (ii) removal of unbound proteins; (iii) elution of proteins adsorbed on gold surfaces using SDS 1 % w/v and (iv) profile analysis of eluted proteins by 1D-electrophoresis. The experiment was performed normalizing the amount of gold material in each sample to the surface area of the laminae (1.5 cm^2). Therefore, different amounts of nanoparticles were used depending on AuNP size: 0.03 mg of 10-cAuNP and 10-pAuNP, 0.18 mg of 60-cAuNP and 60-pAuNP, 0.60 mg of 200-cAuNP and 200-pAuNP. Nanoparticles were added to 1.5 ml PPP solution at physiological concentration. A tube without AuNP was used as negative control.

Planar gold surfaces were placed in 24-wells TCP and incubated with 500 μl plasma solution. Samples were incubated 15 min at 37°C.

To separate unbound proteins from gold materials, two different methods were used for AuNP and planar surfaces, respectively.

Four centrifugation steps (30 min at 18,000 g) were applied to AuNP samples.

After washing procedure, the samples were incubated in 750 µl of SDS 1 % w/v for 1 h at 37°C, then 700 µl supernatants were collected and stored at -20°C before electrophoretic analysis.

The desorbed protein samples were suspended in LDS sample buffer with 1x reducing agent (Nu- PAGETM, Invitrogen) and loaded on acrylamide SDSPAGE gel (NUPage Novex 3-8 %, Tris–acetate). The gel was run at 150 V of constant voltage. After electrophoretic run, the gel was stained using a ProteoSilverTM Silver Staining Kit and digitalized by a GEL LOGIC 200 (Kodak) imaging system.

Results

SEM images of cAuNP (Fig. A1) showed a good matching between nominal size and measured diameter. The data acquired by DLS revealed a size increase of pAuNP with respect to cAuNP confirming the presence of polymer coating on pAuNP. The thickness of PEG coating was in the range from 5 to 10 nm.

The XPS spectra of bare and PEGylated laminae are reported in Fig. A2. The data denoted a large difference in intensity between the peaks at 84 eV of bare and PEGylated surfaces. These peaks were referred to the concentration of metallic gold

on the outer surface of the samples. In correspondence to the decrease of the gold peak, two new components placed at 286 eV and 532 eV, correspondent to carbon and oxygen are found. These outcomes confirm the presence of PEG coating on planar surfaces.
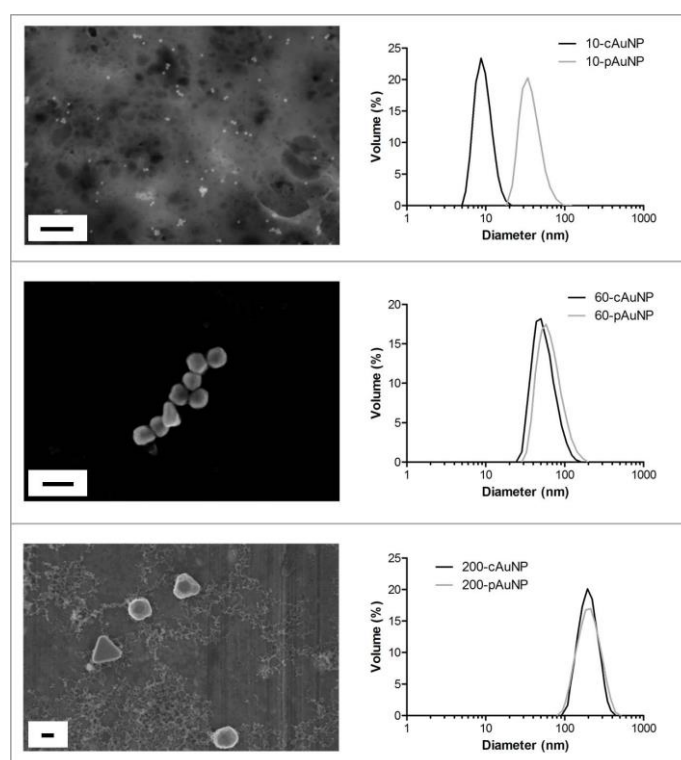

Figure A1. The rows are related to 10, 60 and 200 nm nanoparticles respectively. The left column report the SEM images acquired using cAu (100 nm bar). On the right, the size distributions related to citrate-coated and PEG-coated AuNP suspended in water are reported.
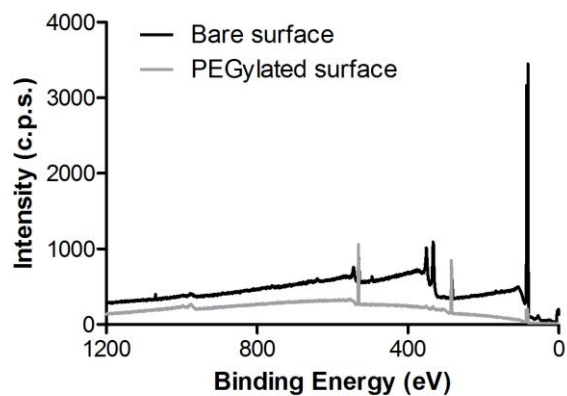
Figure A2. XPS analysis of bare (*black line*) and PEG-coated (*gray line*) gold laminae

Size distribution trends before and after incubation with protein solutions (plasma and HSA) are reported in Fig. A3. It is possible to underline that a more consistent size increase was shown for nanoparticles incubated with plasma respect to AuNP incubated with HSA. In addition, the data suggested that PEG coating is more efficient than citrate in reducing the thickness of protein corona, especially for 60-pAuNP.
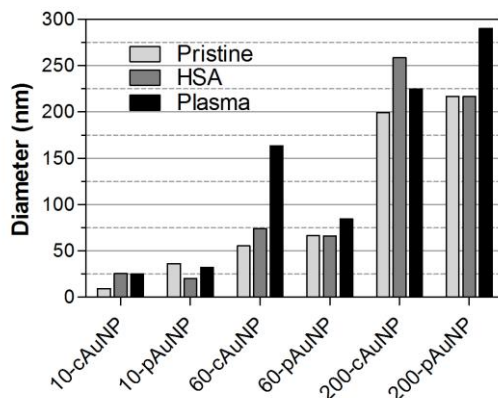
Figure A3. Mean values of the peak related to non-clustered particles in size distributions acquired using DLS. The data are referred to cAuNP and pAuNP incubated in water (pristine), HSA solution (1.0 mg/ml) and platelet-poor plasma solution (physiological concentration), respectively

Different methods have been tested to detach adsorbed proteins from AuNP surface, using SDS 0.1 % w/v, 8 M urea and isopropyl alcohol:NaOH (2:3; isopropyl alcohol 99.5 %: 50 mM NaOH). The results of protein desorption by the different media are presented in Fig. A4. Residual proteins attached to AuNP after the elution processes and proteins desorbed by different agents were quantified using a fluorescence assay. The analysis of fluorescence signals provided by AuNP protein corona after the elution process (Fig. A4.a) provided a ranking of the various desorption media, assuming that a higher fluorescence signal was related to a

thicker residual protein layer due to ineffective desorption. The different eluting media presented an increasing desorption efficacy starting from SDS 0.1 % w/v (14 %) to 8 M urea (36 %) and isopropyl alcohol:NaOH (60 %) if normalized to positive control obtained by AuNP incubation with PBS. This trend was confirmed by direct quantification of the amount of desorbed proteins following elution, reported in Fig. A4.b. In this case, the more effective eluting media provided higher signal, since the amount of protein in the eluted solution depends on the efficacy of the desorption process.

Although being the most efficacious among tested media for protein detachment, NaOH completely disrupts proteins, leading to the impossibility of recognizing the specific bands in the electrophoresis gels. Therefore, because 8 M urea may interfere with electrophoresis running, SDS was selected as eluting medium for the following protein adsorption studies. The surfactant concentration was increased to 1 %w/v to improve desorption efficacy without affecting SDSPAGE analysis.

The electrophoretic bands of proteins desorbed from plasma-incubated gold materials (AuNP and planar surfaces), having a normalized surface area of 1.5 cm^2, are reported in Fig. A5. No remarkable differences between PEGylated and non-PEGylated materials were observed. The comparison between planar surfaces and nanoparticles indicated that the bands related to laminae presented a slightly lower intensity with respect to AuNP bands. Moreover, 200 nm AuNP denoted a higher

protein adsorption if compared to 10 and 60 nm AuNP. The presence of a small fraction of heavy proteins (500 kDa ca.) was observed for AuNP samples, while no traces were revealed in the case of planar surfaces.
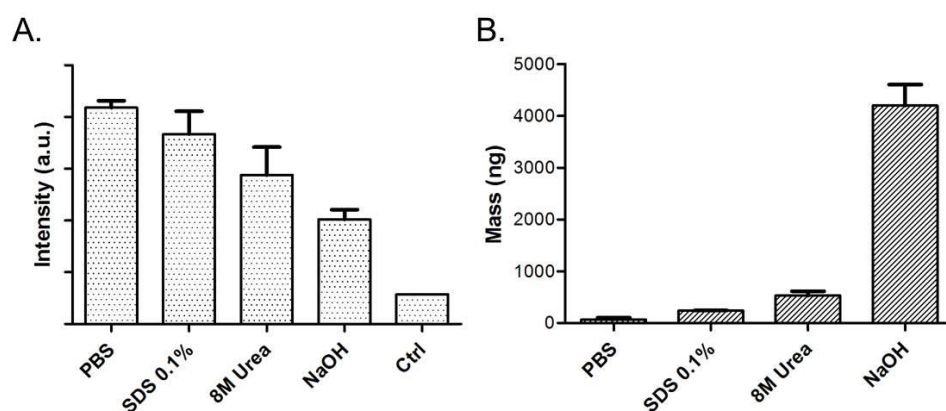

Figure A4. The graph A provides the fluorescence signal of 10-cAuNP after incubation in HSA solution (5.0 mg/ml) and elution using different buffer solutions (PBS at physiological concentration, SDS 0.1 % w/w, 8 M urea, isopropyl alcohol:NaOH). The control is referred to the signal provided by only nanoparticles in ultrapure water. Graph B shows the mass of proteins desorbed through the different eluting processes
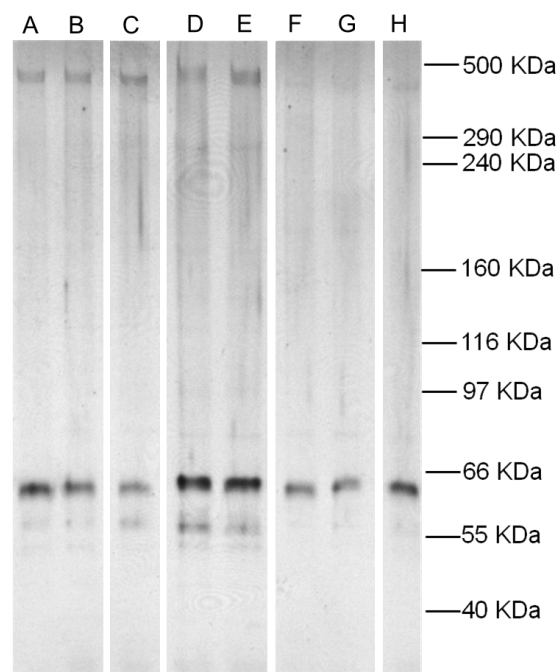
Figure A5. Electrophoretic gel stained by Silver staining. The labels of bands are listed and related to the samples as follows: 10-cAuNP (A), 10-pAuNP (B), 60-cAuNP (C), 200-cAuNP (D), 200-pAuNP (E), bare planar surface (F), PEGylated planar surface (G), negative control (H)

Discussion

Electrophoresis analysis confirmed the presence of heavy proteins on cAuNP protein corona, even if in a lower amount if compared to light proteins, which we consider responsible for nanoparticle stability in solution. This result was in accordance with previous studies[102,103]. When considering SDS-PAGE results, we

can generally observe that the bands related to planar surfaces are less intense with respect to the bands related to AuNP. The higher amount of proteins adsorbed to AuNP can be due to the higher AuNP surface reactivity. This, in turn, could be related to a higher protein binding strength, especially on citratecoated AuNP.

The tendency of PEGylated AuNP to expose a thinner protein corona respect to citrate-coated AuNP can be related to PEG antifouling properties. DLS data about the size distribution of AuNP incubated with plasma and HSA confirming this hypothesis, in accordance with Walkey et al[103]. This result is in contrast with the evidence provided by electrophoresis, which showed similar band intensities for citrate-coated and PEGylated materials. This discordance could be explained assuming that the desorption procedure may have a different effect on PEGylated and non-PEGylated materials, due to a different action of surfactant molecules. It is, in fact, possible that SDS exerts a more effective detaching action on PEGcoated surfaces, which are specifically designed to minimize protein BE, respect to citrate-coated and bare materials. This may induce an overestimation of proteins on PEG-coated samples respect to non- PEGylated ones.

One of the most critical point of the work consists in the high background signal in the NU-PAGE gel. Despite a great accuracy, the protocol was insufficient to reach a satisfactory signal-to-noise ratio to detect fine differences between the materials under investigation. The most probable reasons stand in the relatively small value of

surface area used for the tests or in the scarce removal efficacy of soluble unbound proteins. Differently from other literature studies[103], in our experiments, the value of surface area available for protein adsorption experiments was specifically selected to allow the comparison between AuNP and planar surfaces. Therefore, the parameters used in the present study were optimized to permit the normalization of surface area values. A further increase in surface available for the adsorption tests would have led to the employ of an enormous amount of material. Beside the low signal-to-noise ratio obtained in the case of electrophoretic analysis, the use of a protocol involving protein detachment from AuNP is necessary to investigate protein adsorption on AuNP. The use of standard assays or direct methods for the precise quantification of adsorbed proteins based on the optical (and fluorescence) analyses is, in fact, inappropriate in the case of gold materials because it can generate artifacts related to the fluorescence quenching and unfolding effects induced in proteins by interaction with gold particles[104].

We showed that proteins desorption from AuNP is a critical point that needs to be considered. In fact, the most effective among protein desorption media tested in this study, isopropyl alcohol:NaOH solution, induced simply a partial protein desorption, in the order of 60 %. The other media tested (8 M urea and

SDS 0.1 %w/v) achieved even lower desorption ratios (about 36 and 18 %). Additional care should be used in the choice of eluting media not interfering with the

following analysis. These issues should be carefully considered in the interpretation of past and future studies about protein adsorption to nanomaterials.

In conclusion, we demonstrated the enhancement of surface reactivity from planar to nano-curved materials, showing how this affects complex phenomena like protein adsorption to the surfaces.

A deep knowledge of biological effects of NP upon injection in the blood system is requested to develop safe and effective nanomaterials. This work represents a starting point for the understanding of complex interactions at the molecular level between blood and gold nanomaterials for medical applications.

References

(1)   Vert, M.; Doi, Y.; Hellwich, K.-H.; Hess, M.; Hodge, P.; Kubisa, P.; Rinaudo, M.; Schué, F. Terminology for Biorelated Polymers and Applications (IUPAC Recommendations 2012). *J. Pure Appl. Chem.* **2012**, *84*, 377–410.

(2)   Heiligtag, F. J.; Niederberger, M. The Fascinating World of Nanoparticle Research. *Mater. Today* **2013**, *16*, 262–271.

(3)   Dabbousi, B. O.; Rodriguez-Viejo; Mikulec, F. V; Heine, J. R.; Mattoussi, H.; Ober, R.; Jensen, K. F.; Bawendi, M. G. (CdSe)ZnS Core−Shell Quantum Dots: Synthesis and Characterization of a Size Series of Highly Luminescent Nanocrystallites. *J Phys. Chem. B* **1997**, *101*, 9463–9475.

(4)   Jiles, D. *Introduction to Magnetism and Magnetic Materials*; Chapman and Hall: London, 1991.

(5)   Eustis, S.; el-Sayed, M. A. Why Gold Nanoparticles Are More Precious than Pretty Gold: Noble Metal Surface Plasmon Resonance and Its Enhancement of the Radiative and Nonradiative Properties of Nanocrystals of Different Shapes. *Chem Soc Rev* **2006**, *35*, 209–217.

(6)   Auffan, M.; Rose, J.; Bottero, J. Y.; Lowry, G. V; Jolivet, J. P.; Wiesner, M. R. Towards a Definition of Inorganic Nanoparticles from an Environmental, Health and Safety Perspective. *Nat Nanotechnol* **2009**, *4*, 634–641.

(7)   Murthy, S. K. Nanoparticles in Modern Medicine: State of the Art and Future Challenges. *Int J Nanomedicine* **2007**, *2*, 129–141.

(8)   Davis, M. E.; Chen, Z. G.; Shin, D. M. Nanoparticle Therapeutics: An Emerging Treatment Modality for Cancer. *Nat Rev Drug Discov* **2008**, *7*, 771–782.

(9)   Cedervall, T.; Lynch, I.; Lindman, S.; Berggard, T.; Thulin, E.; Nilsson, H.;

Dawson, K. A.; Linse, S. Understanding the Nanoparticle-Protein Corona Using Methods to Quantify Exchange Rates and Affinities of Proteins for Nanoparticles. *Proc Natl Acad Sci U S A* **2007**, *104*, 2050–2055.

(10)   Gorbet, M. B.; Sefton, M. V. Biomaterial-Associated Thrombosis: Roles of Coagulation Factors, Complement, Platelets and Leukocytes. *Biomaterials* **2004**, *25*, 5681–5703.

(11)   Benetti, F.; Fedel, M.; Minati, L.; Speranza, G.; Migliaresi, C. Gold Nanoparticles: Role of Size and Surface Chemistry on Blood Protein Adsorption. *J. Nanoparticle Res.* **2013**, *15*, 1694–1703.

(12)   Lead, J. R.; Smith, E. *Environmental and Human Health Impacts of Nanotechnology*; Wiley: Chichester, West Sussex, U.K. ; Hoboken, N.J., 2009.

(13)   Tkachenko, A. G.; Xie, H.; Coleman, D.; Glomm, W.; Ryan, J.; Anderson, M. F.; Franzen, S.; Feldheim, D. L. Multifunctional Gold Nanoparticle-Peptide Complexes for Nuclear Targeting. *J Am Chem Soc* **2003**, *125*, 4700–4701.

(14)   Kettler, K.; Veltman, K.; van de Meent, D.; van Wezel, A.; Hendriks, A. J. Cellular Uptake of Nanoparticles as Determined by Particle Properties, Experimental Conditions, and Cell Type. *Env. Toxicol Chem* **2014**, *33*, 481–492.

(15)   Aderem, A.; Underhill, D. M. Mechanisms of Phagocytosis in Macrophages. *Annu Rev Immunol* **1999**, *17*, 593–623.

(16)   Patel, L. N.; Zaro, J. L.; Shen, W. C. Cell Penetrating Peptides: Intracellular Pathways and Pharmaceutical Perspectives. *Pharm Res* **2007**, *24*, 1977–1992.

(17)   Jiang, W.; Kim, B. Y.; Rutka, J. T.; Chan, W. C. Nanoparticle-Mediated Cellular Response Is Size-Dependent. *Nat Nanotechnol* **2008**, *3*, 145–150.

(18)   He, C.; Hu, Y.; Yin, L.; Tang, C.; Yin, C. Effects of Particle Size and Surface Charge on Cellular Uptake and Biodistribution of Polymeric Nanoparticles. *Biomaterials* **2010**, *31*, 3657–3666.

(19)   Lorenz, M. R.; Holzapfel, V.; Musyanovych, A.; Nothelfer, K.; Walther, P.; Frank, H.; Landfester, K.; Schrezenmeier, H.; Mailander, V. Uptake of Functionalized, Fluorescent-Labeled Polymeric Particles in Different Cell Lines and Stem Cells. *Biomaterials* **2006**, *27*, 2820–2828.

(20)   Lewinski, N.; Colvin, V.; Drezek, R. Cytotoxicity of Nanoparticles. *Small* **2008**, *4*, 26–49.

(21)   Choi, S.; Park, J. H.; Jang, S. H.; Lee, H.; Lee, K.; Ryu, P. D.; Yang, S. I.; Joo, S.-W.; Lee, S. Y. Surface-Charge Induced Cellular Uptake and Cytotoxicity of Gold Nanoparticles. *25*.

(22)   Terentyuk, G. S.; Maslyakova, G. N.; Suleymanova, L. V; Khlebtsov, B. N.; Kogan, B. Y.; Akchurin, G. G.; Shantrocha, A. V; Maksimova, I. L.; Khlebtsov, N. G.; Tuchin, V. V. Circulation and Distribution of Gold Nanoparticles and Induced Alterations of Tissue Morphology at Intravenous Particle Delivery. *J Biophotonics* **2009**, *2*, 292–302.

(23)   Hirn, S.; Semmler-Behnke, M.; Schleh, C.; Wenk, A.; Lipka, J.; Schaffler, M.; Takenaka, S.; Moller, W.; Schmid, G.; Simon, U.; *et al.* Particle Size-Dependent and Surface Charge-Dependent Biodistribution of Gold Nanoparticles after Intravenous Administration. *Eur J Pharm Biopharm* **2011**, *77*, 407–416.

(24)   Perrault, S. D.; Walkey, C.; Jennings, T.; Fischer, H. C.; Chan, W. C. Mediating Tumor Targeting Efficiency of Nanoparticles through Design. *Nano Lett* **2009**, *9*, 1909–1915.

(25)   Fraga, S.; Brandao, A.; Soares, M. E.; Morais, T.; Duarte, J. A.; Pereira, L.; Soares, L.; Neves, C.; Pereira, E.; Bastos Mde, L.; *et al.* Short- and Long-Term Distribution and Toxicity of Gold Nanoparticles in the Rat after a Single-Dose Intravenous Administration. *Nanomedicine* **2014**, *10*, 1757–1766.

(26)   Lee, P. W.; Hsu, S. H.; Wang, J. J.; Tsai, J. S.; Lin, K. J.; Wey, S. P.; Chen, F. R.; Lai, C. H.; Yen, T. C.; Sung, H. W. The Characteristics, Biodistribution, Magnetic Resonance Imaging and Biodegradability of Superparamagnetic Core-Shell Nanoparticles. *Biomaterials* **2010**, *31*, 1316–1324.

(27) Cole, A. J.; David, A. E.; Wang, J.; Galban, C. J.; Yang, V. C. Magnetic Brain Tumor Targeting and Biodistribution of Long-Circulating PEG-Modified, Cross-Linked Starch-Coated Iron Oxide Nanoparticles. *Biomaterials* **2011**, *32*, 6291–6301.

(28) Tate, J. A.; Petryk, A. A.; Giustini, A. J.; Hoopes, P. J. Biodistribution of Iron Oxide Nanoparticles: An Overview. *Proc SPIE Int Soc Opt Eng* **2011**, *7901*, 790117.

(29) Fang, J.; Nakamura, H.; Maeda, H. The EPR Effect: Unique Features of Tumor Blood Vessels for Drug Delivery, Factors Involved, and Limitations and Augmentation of the Effect. *Adv Drug Deliv Rev* **2011**, *63*, 136–151.

(30) Iyer, A. K.; Khaled, G.; Fang, J.; Maeda, H. Exploiting the Enhanced Permeability and Retention Effect for Tumor Targeting. *Drug Discov Today* **2006**, *11*, 812–818.

(31) Torchilin, V. P. Recent Advances with Liposomes as Pharmaceutical Carriers. *Nat Rev Drug Discov* **2005**, *4*, 145–160.

(32) Nida, D. L.; Rahman, M. S.; Carlson, K. D.; Richards-Kortum, R.; Follen, M. Fluorescent Nanocrystals for Use in Early Cervical Cancer Detection. *Gynecol Oncol* **2005**, *99*, S89–S94.

(33) Wang, H. Z.; Wang, H. Y.; Liang, R. Q.; Ruan, K. C. Detection of Tumor Marker CA125 in Ovarian Carcinoma Using Quantum Dots. *Acta Biochim Biophys Sin* **2004**, *36*, 681–686.

(34) Wu, X.; Liu, H.; Liu, J.; Haley, K. N.; Treadway, J. A.; Larson, J. P.; Ge, N.; Peale, F.; Bruchez, M. P. Immunofluorescent Labeling of Cancer Marker Her2 and Other Cellular Targets with Semiconductor Quantum Dots. *Nat Biotechnol* **2003**, *21*, 41–46.

(35) Cuenca, A. G.; Jiang, H.; Hochwald, S. N.; Delano, M.; Cance, W. G.; Grobmyer, S. R. Emerging Implications of Nanotechnology on Cancer Diagnostics and Therapeutics. *Cancer* **2006**, *107*, 459–466.

(36)   Terentyuk, G. S.; Maslyakova, G. N.; Suleymanova, L. V; Khlebtsov, N. G.; Khlebtsov, B. N.; Akchurin, G. G.; Maksimova, I. L.; Tuchin, V. V. Laser-Induced Tissue Hyperthermia Mediated by Gold Nanoparticles: Toward Cancer Phototherapy. *J. Biomed. Opt.* **2009**, *14*, 21016–21019.

(37)   Huang, X.; Jain, P.; El-Sayed, I.; El-Sayed, M. Plasmonic Photothermal Therapy (PPTT) Using Gold Nanoparticles. *Lasers Med. Sci.* **2008**, *23*, 217–228.

(38)   Grobmyer, Q. Z. and N. I. and P. S. and B. M. M. and C. W. and J. M. and H. J. and S. R. Gold Nanoparticles as a Contrast Agent for in Vivo Tumor Imaging with Photoacoustic Tomography. *Nanotechnology* **2009**, *20*, 395102.

(39)   Gómez-Lopera, S. A.; Plaza, R. C.; Delgado, A. V. Synthesis and Characterization of Spherical Magnetite/Biodegradable Polymer Composite Particles. *J. Colloid Interface Sci.* **2001**, *240*, 40–47.

(40)   Goodwin, S.; Peterson, C.; Hoh, C.; Bittner, C. Targeting and Retention of Magnetic Targeted Carriers (MTCs) Enhancing Intra-Arterial Chemotherapy. *J. Magn. Magn. Mater.* **1999**, *194*, 132–139.

(41)   Goodwin, S. C.; Bittner, C. A.; Peterson, C. L.; Wong, G. Single-Dose Toxicity Study of Hepatic Intra-Arterial Infusion of Doxorubicin Coupled to a Novel Magnetically Targeted Drug Carrier. *Toxicol. Sci.* **2001**, *60* , 177–183.

(42)   Pulfer, S.; Gallo, J. Enhanced Brain Tumor Selectivity of Cationic Magnetic Polysaccharide Microspheres. *J. Drug Target.* **1998**, *6*, 215–227.

(43)   Pulfer, S.; Ciccotto, S.; Gallo, J. Distribution of Small Magnetic Particles in Brain Tumor-Bearing Rats. *J. Neurooncol.* **1999**, *41*, 99–105.

(44)   Michel, S. C. A.; Keller, T. M.; Fröhlich, J. M.; Fink, D.; Caduff, R.; Seifert, B.; Marincek, B.; Kubik-Huch, R. A. Preoperative Breast Cancer Staging: MR Imaging of the Axilla with Ultrasmall Superparamagnetic Iron Oxide Enhancement. *Radiology* **2002**, *225*, 527–536.

(45)   Enochs, W. S.; Harsh, G.; Hochberg, F.; Weissleder, R. Improved Delineation of Human Brain Tumors on MR Images Using a Long-Circulating,

Superparamagnetic Iron Oxide Agent. *J. Magn. Reson. Imaging* **1999**, *9*, 228–232.

(46)   Semelka, R. C.; Helmberger, T. K. G. Contrast Agents for MR Imaging of the Liver. *Radiology* **2001**, *218*, 27–38.

(47)   Moroz, P.; Jones, S. K.; Winter, J.; Gray, B. N. Targeting Liver Tumors with Hyperthermia: Ferromagnetic Embolization in a Rabbit Liver Tumor Model. *J. Surg. Oncol.* **2001**, *78*, 22–29.

(48)   Minamimura, T.; Sato, H.; Kasaoka, S.; Saito, T.; Ishizawa, S.; Takemori, S.; Tazawa, K.; Tsukada, K. Tumor Regression by Inductive Hyperthermia Combined with Hepatic Embolization Using Dextran Magnetite-Incorporated Microspheres in Rats. *Int. J. Oncol.* **2000**, *16*, 1153–1161.

(49)   Jonesa, S.; Wintera, J.; Graya, B. Treatment of Experimental Rabbit Liver Tumours by Selectively Targeted Hyperthermia. *Int. J. Hyperth.* **2002**, *18*, 117–128.

(50)   DeNardo, G. L.; DeNardo, S. J. Concepts, Consequences, and Implications of Theranosis. *Semin. Nucl. Med.* **2012**, *42*, 147–150.

(51)   Gautier, J.; Allard-Vannier, E.; Munnier, E.; Soucé, M.; Chourpa, I. Recent Advances in Theranostic Nanocarriers of Doxorubicin Based on Iron Oxide and Gold Nanoparticles. *J. Control. Release* **2013**, *169*, 48–61.

(52)   Hayashi, K.; Nakamura, M.; Sakamoto, W.; Yogo, T.; Miki, H.; Ozaki, S.; Abe, M.; Matsumoto, T.; Ishimura, K. Superparamagnetic Nanoparticle Clusters for Cancer Theranostics Combining Magnetic Resonance Imaging and Hyperthermia Treatment. *Theranostics* **2013**, *3*, 366–376.

(53)   Joh, D. Y.; Kao, G. D.; Murty, S.; Stangl, M.; Sun, L.; Zaki, A. Al; Xu, X.; Hahn, S. M.; Tsourkas, A.; Dorsey, J. F. Theranostic Gold Nanoparticles Modified for Durable Systemic Circulation Effectively and Safely Enhance the Radiation Therapy of Human Sarcoma Cells and Tumors. *Transl. Oncol.* **2013**, *6*, 722–IN32.

(54)   Lux, F.; Sancey, L.; Bianchi, A.; Crémillieux, Y.; Roux, S.; Tillement, O.

Gadolinium-Based Nanoparticles for Theranostic MRI-Radiosensitization. *Nanomedicine* **2015**, *10*, 1801–1815.

(55) Kirui, D. K.; Khalidov, I.; Wang, Y.; Batt, C. A. Targeted near-IR Hybrid Magnetic Nanoparticles for in Vivo Cancer Therapy and Imaging. *Nanomedicine Nanotechnology, Biol. Med.* **2013**, *9*, 702–711.

(56) Kim, J.; Kim, H. S.; Lee, N.; Kim, T.; Kim, H.; Yu, T.; Song, I. C.; Moon, W. K.; Hyeon, T. Multifunctional Uniform Nanoparticles Composed of a Magnetite Nanocrystal Core and a Mesoporous Silica Shell for Magnetic Resonance and Fluorescence Imaging and for Drug Delivery. *Angew. Chemie* **2008**, *120*, 8566–8569.

(57) S, T. The Role of Radiotherapy in the Management of Cancer--an Overview. *Ann. Acad. Med. Singapore* **1996**, *25*, 371–379.

(58) Delaney, G.; Jacob, S.; Featherstone, C.; Barton, M. The Role of Radiotherapy in Cancer Treatment. *Cancer* **2005**, *104*, 1129–1137.

(59) Joiner, M.; Kogel, A.; Steel, G. Introduction: The Significance of Radiobiology and Radiotherapy for Cancer Treatment. In *Basic Clinical Radiobiology*; 2009.

(60) Wouters, B.; Begg, A. Irradiation-Induced Damage and the DNA Damage Response. In *Basic Clinical Radiobiology*; 2009.

(61) Wardman, P. Chemical Radiosensitizers for Use in Radiotherapy. *Clin. Oncol. (R. Coll. Radiol).* **2007**, *19*, 397–417.

(62) Moding, E. J.; Kastan, M. B.; Kirsch, D. G. Strategies for Optimizing the Response of Cancer and Normal Tissues to Radiation. *Nat Rev Drug Discov* **2013**, *12*, 526–542.

(63) Hubbell, J.; Seltzer, S. Tables of X-Ray Mass Attenuation Coefficients and Mass Energy-Absorption Coefficients from 1 keV to 20 MeV for Elements Z = 1 to 92 and 48 Additional Substances of Dosimetric Interest, 1996.

(64) Carter, J. D.; Cheng, N. N.; Qu, Y.; Suarez, G. D.; Guo, T. Nanoscale Energy

Deposition by X-Ray Absorbing Nanostructures. *J. Phys. Chem. B* **2007**, *111*, 11622–11625.

(65)   Zhang, S.; Gao, J.; Buchholz, T.; Wang, Z.; Salehpour, M.; Drezek, R.; Yu, T.-K. Quantifying Tumor-Selective Radiation Dose Enhancements Using Gold Nanoparticles: A Monte Carlo Simulation Study. *Biomed. Microdevices* **2009**, *11*, 925–933.

(66)   McMahon, S. J.; Hyland, W. B.; Muir, M. F.; Coulter, J. A.; Jain, S.; Butterworth, K. T.; Schettino, G.; Dickson, G. R.; Hounsell, A. R.; O'Sullivan, J. M.; *et al.* Nanodosimetric Effects of Gold Nanoparticles in Megavoltage Radiation Therapy. *Radiother. Oncol.* **2011**, *100*, 412–416.

(67)   Hainfeld, J. F.; Slatkin, D. N.; Smilowitz, H. M. The Use of Gold Nanoparticles to Enhance Radiotherapy in Mice. *Phys. Med. Biol.* **2004**, *49*, N309.

(68)   Jain, S.; Coulter, J. A.; Hounsell, A. R.; Butterworth, K. T.; McMahon, S. J.; Hyland, W. B.; Muir, M. F.; Dickson, G. R.; Prise, K. M.; Currell, F. J.; *et al.* Cell-Specific Radiosensitization by Gold Nanoparticles at Megavoltage Radiation Energies. *Int. J. Radiat. Oncol. Biol. Phys.* **2011**, *79*, 531–539.

(69)   Wolfe, T.; Chatterjee, D.; Lee, J.; Grant, J. D.; Bhattarai, S.; Tailor, R.; Goodrich, G.; Nicolucci, P.; Krishnan, S. Targeted Gold Nanoparticles Enhance Sensitization of Prostate Tumors to Megavoltage Radiation Therapy in Vivo. *Nanomedicine* **2015**, *11*, 1277–1283.

(70)   Zhang, X.-D.; Wu, D.; Shen, X.; Chen, J.; Sun, Y.-M.; Liu, P.-X.; Liang, X.-J. Size-Dependent Radiosensitization of PEG-Coated Gold Nanoparticles for Cancer Radiation Therapy. *Biomaterials* **2012**, *33*, 6408–6419.

(71)   Darwish, A.; Blacker, M.; Janzen, N.; Rathmann, S. M.; Czorny, S.; Hillier, S. M.; Joyal, J. L.; Babich, J. W.; Valliant, J. F. Triazole Appending Agent (TAAG): A New Synthon for Preparing Iodine-Based Molecular Imaging and Radiotherapy Agents. *ACS Med. Chem. Lett.* **2012**, *3*, 313–316.

(72)   Kettering, M.; Zorn, H.; Bremer-Streck, S.; Oehring, H.; Zeisberger, M.; Bergemann, C.; Hergt, R.; Halbhuber, K.-J.; Kaiser, W. A.; Hilger, I.

Characterization of Iron Oxide Nanoparticles Adsorbed with Cisplatin for Biomedical Applications. *Phys. Med. Biol.* **2009**, *54*, 5109.

(73) Huang, C.; Neoh, K. G.; Xu, L.; Kang, E. T.; Chiong, E. Polymeric Nanoparticles with Encapsulated Superparamagnetic Iron Oxide and Conjugated Cisplatin for Potential Bladder Cancer Therapy. *Biomacromolecules* **2012**, *13*, 2513–2520.

(74) Le Duc, G.; Miladi, I.; Alric, C.; Mowat, P.; Bräuer-Krisch, E.; Bouchet, A.; Khalil, E.; Billotey, C.; Janier, M.; Lux, F.; *et al.* Toward an Image-Guided Microbeam Radiation Therapy Using Gadolinium-Based Nanoparticles. *ACS Nano* **2011**, *5*, 9566–9574.

(75) Dufort, S.; Bianchi, A.; Henry, M.; Lux, F.; Le Duc, G.; Josserand, V.; Louis, C.; Perriat, P.; Crémillieux, Y.; Tillement, O.; *et al.* Nebulized Gadolinium-Based Nanoparticles: A Theranostic Approach for Lung Tumor Imaging and Radiosensitization. *Small* **2015**, *11*, 215–221.

(76) Luchette, M.; Korideck, H.; Makrigiorgos, M.; Tillement, O.; Berbeco, R. Radiation Dose Enhancement of Gadolinium-Based AGuIX Nanoparticles on HeLa Cells. *Nanomedicine* **2014**, *10*, 1751–1755.

(77) Alric, C.; Taleb, J.; Duc, G. Le; Mandon, C.; Billotey, C.; Meur-Herland, A. Le; Brochard, T.; Vocanson, F.; Janier, M.; Perriat, P.; *et al.* Gadolinium Chelate Coated Gold Nanoparticles As Contrast Agents for Both X-Ray Computed Tomography and Magnetic Resonance Imaging. *J. Am. Chem. Soc.* **2008**, *130*, 5908–5915.

(78) Kim, H.-K.; Jung, H.-Y.; Park, J.-A.; Huh, M.-I.; Jung, J.-C.; Chang, Y.; Kim, T.-J. Gold Nanoparticles Coated with Gadolinium-DTPA-Bisamide Conjugate of Penicillamine (Au@GdL) as a T1-Weighted Blood Pool Contrast Agent. *J. Mater. Chem.* **2010**, *20*, 5411–5417.

(79) Irure, A.; Marradi, M.; Arnaiz, B.; Genicio, N.; Padro, D.; Penades, S. Sugar/gadolinium-Loaded Gold Nanoparticles for Labelling and Imaging Cells by Magnetic Resonance Imaging. *Biomater. Sci.* **2013**, *1*, 658–668.

(80) Minati, L.; Benetti, F.; Chiappini, A.; Speranza, G. One-Step Synthesis of

Star-Shaped Gold Nanoparticles. *Colloids Surfaces A Physicochem. Eng. Asp.* **2014**, *441*, 623–628.

(81) Okamoto, T.; Yamaguchi, I. Optical Absorption Study of the Surface Plasmon Resonance in Gold Nanoparticles Immobilized onto a Gold Substrate by Self-Assembly Technique. *J. Phys. Chem. B* **2003**, *107*, 10321–10324.

(82) Ghosh, S. K.; Pal, T. Interparticle Coupling Effect on the Surface Plasmon Resonance of Gold Nanoparticles: From Theory to Applications. *Chem. Rev.* **2007**, *107*, 4797–4862.

(83) Sun, S.; Zeng, H.; Robinson, D. B.; Raoux, S.; Rice, P. M.; Wang, S. X.; Li, G. Monodisperse MFe2O4 (M = Fe, Co, Mn) Nanoparticles. *J. Am. Chem. Soc.* **2004**, *126*, 273–279.

(84) Tong, S.; Hou, S.; Ren, B.; Zheng, Z.; Bao, G. Self-Assembly of Phospholipid–PEG Coating on Nanoparticles through Dual Solvent Exchange. *Nano Lett.* **2011**, *11*, 3720–3726.

(85) Yu, H.; Chen, M.; Rice, P. M.; Wang, S. X.; White, R. L.; Sun, S. Dumbbell-like Bifunctional Au−Fe3O4 Nanoparticles. *Nano Lett.* **2005**, *5*, 379–382.

(86) Jin, X.; Liang, J.; Yang, C.; Hao, R.; Zhuang, J.; Yang, W. Facile Deposition of Continuous Gold Shells on Tween-20 Modified Fe3O4 Superparticles. *J. Mater. Chem. B* **2013**, *1*, 1921–1925.

(87) Zhang, L.; He, R.; Gu, H.-C. Oleic Acid Coating on the Monodisperse Magnetite Nanoparticles. *Appl. Surf. Sci.* **2006**, *253*, 2611–2617.

(88) Xu, C.; Xie, J.; Ho, D.; Wang, C.; Kohler, N.; Walsh, E. G.; Morgan, J. R.; Chin, Y. E.; Sun, S. Au–Fe3O4 Dumbbell Nanoparticles as Dual-Functional Probes. *Angew. Chemie Int. Ed.* **2008**, *47*, 173–176.

(89) Kirui, D. K.; Rey, D. A.; Batt, C. A. Gold Hybrid Nanoparticles for Targeted Phototherapy and Cancer Imaging. *Nanotechnology* **2010**, *21*, 105105.

(90) Maity, D.; Chandrasekharan, P.; Pradhan, P.; Chuang, K.-H.; Xue, J.-M.; Feng, S.-S.; Ding, J. Novel Synthesis of Superparamagnetic Magnetite

Nanoclusters for Biomedical Applications. *J. Mater. Chem.* **2011**, *21*, 14717–14724.

(91)   Ottaviani, G.; Jaffe, N. The Epidemiology of Osteosarcoma. In *Pediatric and Adolescent Osteosarcoma SE - 1*; Jaffe, N.; Bruland, O. S.; Bielack, S., Eds.; Cancer Treatment and Research; Springer US, 2010; Vol. 152, pp. 3–13.

(92)   Dhule, S. S.; Penfornis, P.; Frazier, T.; Walker, R.; Feldman, J.; Tan, G.; He, J.; Alb, A.; John, V.; Pochampally, R. Curcumin-Loaded γ-Cyclodextrin Liposomal Nanoparticles as Delivery Vehicles for Osteosarcoma. *Nanomedicine Nanotechnology, Biol. Med.* **2012**, *8*, 440–451.

(93)   Popwell, S. J.; Schulz, M. D.; Wagener, K. B.; Batich, C. D.; Milner, R. J.; Lagmay, J.; Bolch, W. E. Synthesis of Polymeric Phosphonates for Selective Delivery of Radionuclides to Osteosarcoma. *Cancer Biother. Radiopharm.* **2014**, *29*, 273–282.

(94)   Fuchs, B.; Pritchard, D. J. Etiology of Osteosarcoma. *Clin. Orthop. Relat. Res.* **2002**, *397*.

(95)   DeLaney, T. F.; Park, L.; Goldberg, S. I.; Hug, E. B.; Liebsch, N. J.; Munzenrider, J. E.; Suit, H. D. Radiotherapy for Local Control of Osteosarcoma. *Int. J. Radiat. Oncol. Biol. Phys.* **2005**, *61*, 492–498.

(96)   Schwarz, R.; Bruland, O.; Cassoni, A.; Schomberg, P.; Bielack, S. The Role of Radiotherapy in Oseosarcoma. In *Pediatric and Adolescent Osteosarcoma SE - 7*; Jaffe, N.; Bruland, O. S.; Bielack, S., Eds.; Cancer Treatment and Research; Springer US, 2010; Vol. 152, pp. 147–164.

(97)   Anoopkumar-Dukie, S.; Carey, J. B.; Conere, T.; O'Sullivan, E.; van Pelt, F. N.; Allshire, A. Resazurin Assay of Radiation Response in Cultured Cells. *Br. J. Radiol.* **2005**, *78*, 945–947.

(98)   Gao, W.; Ji, L.; Li, L.; Cui, G.; Xu, K.; Li, P.; Tang, B. Bifunctional Combined Au-Fe(2)O(3) Nanoparticles for Induction of Cancer Cell-Specific Apoptosis and Real-Time Imaging. *Biomaterials* **2012**, *33*, 3710–3718.

(99)   Landázuri, N.; Tong, S.; Suo, J.; Joseph, G.; Weiss, D.; Sutcliffe, D. J.; Giddens, D. P.; Bao, G.; Taylor, W. R. Magnetic Targeting of Human Mesenchymal Stem Cells with Internalized Superparamagnetic Iron Oxide Nanoparticles. *Small* **2013**, *9*, 4017–4026.

(100) Eskandani, M.; Hamishehkar, H.; Ezzati Nazhad Dolatabadi, J. Cyto/Genotoxicity Study of Polyoxyethylene (20) Sorbitan Monolaurate (Tween 20). *DNA Cell Biol.* **2013**, *32*, 498–503.

(101) Kou, L.; Sun, J.; Zhai, Y.; He, Z. The Endocytosis and Intracellular Fate of Nanomedicines: Implication for Rational Design. *Asian J. Pharm. Sci.* **2013**, *8*, 1–10.

(102) Dobrovolskaia, M. A.; Patri, A. K.; Zheng, J.; Clogston, J. D.; Ayub, N.; Aggarwal, P.; Neun, B. W.; Hall, J. B.; McNeil, S. E. Interaction of Colloidal Gold Nanoparticles with Human Blood: Effects on Particle Size and Analysis of Plasma Protein Binding Profiles. *Nanomedicine Nanotechnology, Biol. Med.* **2009**, *5*, 106–117.

(103) Walkey, C. D.; Olsen, J. B.; Guo, H.; Emili, A.; Chan, W. C. W. Nanoparticle Size and Surface Chemistry Determine Serum Protein Adsorption and Macrophage Uptake. *J. Am. Chem. Soc.* **2012**, *134*, 2139–2147.

(104) Lacerda, S. H. D. P.; Park, J. J.; Meuse, C.; Pristinski, D.; Becker, M. L.; Karim, A.; Douglas, J. F. Interaction of Gold Nanoparticles with Common Human Blood Proteins. *ACS Nano* **2010**, *4*, 365–379.

Scientific Production

F Benetti, D Maniglio, L Minati, J Jovicich, A Valentini, G Speranza, C Migliaresi (2016) Development of theranostic gold-magnetite hybrid nanoparticles for advanced radiotherapy. *Manuscript in preparation*

L Minati, C L Cheng, Y C Lin, J Hees, G Lewes-Malandrakis, C E Nebel, **F Benetti**, C Migliaresi, G Speranza (2015) Synthesis of novel nanodiamonds–gold core shell nanoparticles. *Diamonds and Related Materials*, **53**, 23-28

E Butturini, P Dolcet, M Casarin, A Speghini, M Pedroni, **F Benetti**, A Motta, D Badocco, P Pastore, S Diodati, L Pandolfo, S Gross (2014) Simple, common but functional: biocompatible and luminescent rare-earth doped magnesium and calcium hydroxides from miniemulsion. *Materials Chemistry B*, **2**, 6639-6651

L Minati, **F Benetti**, A Chiappini, G Speranza (2014) One-step synthesis of star-shaped gold nanoparticles. *Colloids and Surfaces A*, **441**, 623-628

F Benetti, L Minati, M Fedel, G Speranza, C Migliaresi (2013) Gold nanoparticles: role of size and surface chemistry on blood protein adsorption, *Nanoparticles Research*, **15**, 1694-170

Participation to Congresses, Schools and Workshops

Congresses:

- **ITNANO 2015, 3rd International Translational Nanomedicine Conference**, Milocer (Montenegro) June 21st-26th, 2015. Best poster award. Poster title: "Development of Theranostic Au-Fe3O4 Nanoparticles for Advanced Radiotherapy".

- **Physics & Medicine: Towards a Future of Integration**, Trento 6th – 8thNovember, 2014. Participation with oral presentation titled "Development of Gold/Iron Oxide Hybrid Nanoparticles for Advanced Radiotherapy".

- **Tissue Engineering & Regenerative Medicine International Symposium**, Genova 10th – 13th June, 2014. Participation with oral presentation titled "Synthesis and Characterization of Gold/Iron Oxide Hybrid Nanoparticles for Multiple Biomedical Applications".

- **Italian Crystal Growth Conference**, Parma 14st– 15th November, 2013. Participation with oral presentation titled "Synthesis and Characterization of Iron Oxide Gold Core/Shell Nanoparticles for CancerCare".

Schools:

- **Winter School: IEEE Italy Career Boosting**, Povo (Trento) 10th – 14th Feb. 2014. Principles of project management.

- **Summer School: Biomaterials and Regenerative Medicine**, Riva del Garda (Trento) 8th – 12th June 2013.

Workshops:

- **Meeting on Industrial Problem Solving with Physics**, Trento 21st – 26th July 2014. One-week teamwork on a real industrial problem proposed by Aquafill Spa (Arco, Trento).
- **Electron-Matter Interaction As A Tool For Materials Analysis: Theory And Experiment**, Povo (Trento) January 29th, 2013.

Acknowledgments